

---

# Weak neural variational inference for solving Bayesian inverse problems *without* forward models: applications in elastography

---

Vincent C. Scholz<sup>a</sup>, Yaohua Zang<sup>a</sup>, Phaedon-Stelios Koutsourelakis<sup>a,b</sup>

<sup>a</sup> Technical University of Munich, Professorship of Data-driven Materials Modeling, School of Engineering and Design, Boltzmannstr. 15, Garching, Germany

<sup>b</sup> Munich Data Science Institute (MDSI - Core member), Garching, Germany  
{vincent.scholz, yaohua.zang, p.s.koutsourelakis}@tum.de

## Abstract

In this paper, we introduce a novel, data-driven approach for solving high-dimensional Bayesian inverse problems based on partial differential equations (PDEs), called Weak Neural Variational Inference (WNVI). The method complements real measurements with virtual observations derived from the physical model. In particular, weighted residuals are employed as probes to the governing PDE in order to formulate and solve a Bayesian inverse problem *without* ever formulating nor solving a forward model. The formulation treats the state variables of the physical model as latent variables, inferred using Stochastic Variational Inference (SVI), along with the usual unknowns. The approximate posterior employed uses neural networks to approximate the inverse mapping from state variables to the unknowns. We illustrate the proposed method in a biomedical setting where we infer spatially varying material properties from noisy tissue deformation data. We demonstrate that WNVI is not only as accurate and more efficient than traditional methods that rely on repeatedly solving the (non)linear forward problem as a black-box, but it can also handle ill-posed forward problems (e.g., with insufficient boundary conditions).

**Keywords** Bayesian Inverse Problem · Weighted Residuals · Virtual likelihood · Variational Inference · Elastography.

## 1 Introduction

Model-based inverse problems enhance our ability to extract information from data by enabling the identification of unknown model parameters or functions. In this manner, one can gain unparalleled insight into the state of the system of interest as well as calibrate associated models to obtain

accurate predictions about the system's evolution. The solution of model-based inverse problems has had significant impact in several fields such as medical imaging [1], climate modeling [2], geophysics [3], and astronomy [4]. One such application is model-based elastography [5], a technique employed in medical imaging to identify the mechanical properties of biological tissue based on tissue deformation data. The latter are obtained with, e.g., ultrasound or MRI and arise from static or time-dependent excitations. The material properties are identified in a non-intrusive manner and provide a characterization of the tissue, which medical practitioners can use to diagnose patients and, in some cases, detect the appearance of pathologies earlier as compared to classical imaging techniques alone (e.g., x-rays, MRI) [6, 7, 8, 9, 10, 11, 12, 13]. In this case, the model consists of the (non)linear Partial Differential Equations (PDEs) of solid mechanics with associated boundary/initial conditions. These are subsequently discretized, and the resulting system of thousands or millions of (non)linear (and potentially time-dependent) algebraic equations constitutes the so-called forward model. While these are commonplace in the engineering mechanics community, the discretization and use of such models is out-of-reach for the majority of medical practitioners. This has been a significant obstacle in the permeation of such techniques despite the wealth of useful information they can furnish. It should also be noted that in several circumstances, the availability of a forward model is not guaranteed. In the simplest case where mild pressure is applied, e.g., on a patient's abdomen with an ultrasound wand, which is used to acquire images of the deformation in the underlying tissue, boundary conditions are in part or in whole, missing [14, 15]. Irrespective of the aforementioned issues and even in cases where a well-posed forward model is available, the solution of the inverse problem requires multiple solutions and derivatives of the model-predicted displacements/strains with respect to the sought parameters. As each call to the forward model solver can be cumbersome, the solution of the inverse problem might be slow and require significant investments in dedicated computing hardware.

The aforementioned difficulties are to various degrees also present in the entirety of PDE-based inverse problems. In combination with the unavoidable noise in the observation data [16] contribute to the well-documented *ill-posedness* of inverse problems [17]. As our formulation is Bayesian in nature we primarily review pertinent techniques [18]. Such formulations do not yield point estimates but rather quantify the probability with which the unknowns take any of the possible values. Bayesian estimates can be of great importance in medical diagnostics in particular as they can guide decision-making and inform the need for more data or tests. Classical probabilistic inference techniques such as MARKOV-chain Monte-Carlo (MCMC) [19], Sequential Monte Carlo (SMC) [20] and Variational Inference (VI) [21] exhibit very poor scaling in terms of the number of forward-model calls with the dimension of the vector of unknowns [22, 23]. As a result, several efforts have been directed toward reducing the intrinsic dimension [24, 25] of the unknowns or reducing the cost of the each forward-model solve. In the latter case, a popular direction involves the development of surrogates for the forward map based on, e.g. polynomial chaos [26, 27], GAUSSian processes [28, 29], reduced-order models [30], deep neural networks [31, 32, 33], neural operators [34, 35, 36] which are frequently employed in multi-fidelity schemes [37, 38, 39]. It is noted that such surrogates have also been proposed for the inverse map [40, 36]. Generally the surrogates are trained in an offline-phase using several input-output pairs which imply an equal number of forward-model solves. Apart from the cost associated with data generation which increases rather fast with the input dimension, the trained

surrogate can introduce bias or additional (epistemic) uncertainty which should be accounted during inference [41]. More importantly perhaps and given that the posterior is generally concentrated on a minute and a-priori unknown region of the parameter space, it becomes questionable whether the surrogate can provide sufficient accuracy in that region.

Physics-informed machine learning tools have more recently been proposed such as PINNs [42], weak adversarial networks [43, 44]), DeepONets [35, 36], PINO [45]. These methods employ collocation residuals of the governing PDE in the training loss and as such can produce solutions to the inverse problem without even solving the forward problem. When the unknowns consist of a spatially-varying property field as in the case of elastography, they express this with a neural network which complicates the incorporation of prior information when this is available. As a result, they have difficulties capturing jumps in the underlying property field as is the case when inclusions-tumors are present in the tissue [46]. In [47, 48], a Bayesian version of PINNs was proposed where a posterior on the weights/biases of the neural network expressing the unknown field is inferred. Although only collocation residuals (and their derivatives) need to be evaluated at each iteration, their total number, and as a result the total computational cost, can be comparable to classical techniques due to the local information they provide and the lack of quantification of their informational content.

In this paper, we build upon previous work [49, 50] that attempts to overcome the tyranny of an expensive black-box solver for the forward model. We propose a probabilistic learning objective in which weighted residuals of the governing PDE are used as *virtual* observables, which are combined with the actual observables via a *virtual* likelihood [51, 52]. Most similar to our method is perhaps the work of [53] who employ all the weighted residuals and a different architecture for synthesising actual observables as well as for inferring the unknown parameters. We show that selecting a few weighted residuals at random at each iteration offers a theoretically consistent formulation that is sufficient to infer the unknown, spatially varying property field and to obtain probabilistic estimates without ever solving the forward model [54]. Our contributions can be summarized as follows:

- we obviate the need for a well-posed forward problem. As such, the formulation can be employed in cases where, e.g., boundary conditions are unknown or insufficiently specified.
- as a further consequence, inference of the posterior does not require any costly forward model evaluations nor adjoint computations for the evaluation of derivatives of the (log-)likelihood. In addition, it eliminates the need for cumbersome discretizations (e.g. finite differences/elements) of the governing equations.
- updates require the evaluation of a reduced number of weighted residuals (and their derivatives), i.e., integrals over the problem domain, which accelerates inference.
- as a result, the solution of inverse problems based on linear or non-linear forward models proceeds identically without the need for methodological adjustments, nor does it imply any additional computational burden.

The subsequent sections of this paper are structured as follows: In Section 2, we introduce the forward and BAYESian inverse problem for elastography. Section 3 outlines our general methodology and derivation of the evidence lower bound (ELBO) necessary for approximating the posterior as well

as the form of approximate posterior. In Section 4, we demonstrate the efficiency of our approach through numerical experiments. Finally, Section 5 concludes with a summary and outlook.

## 2 Problem definition

In this section, we discuss the main aspects of the problem of model-based elastography [55]. In particular, the governing PDEs that constitute the forward model as well as the data based on which one can formulate the Bayesian inverse problem. We note that the essential elements and the resulting challenges are identical for most other PDE-based inverse problems. As mentioned in the introduction, the governing equations arise from solid mechanics and, in particular, the conservation of linear momentum, which, in the case of time-independent settings and the absence of body forces, dictates that:

$$\nabla \cdot \boldsymbol{\sigma}(\mathbf{s}) = 0 \quad \mathbf{s} \in \Omega \subset \mathbb{R}^d, \quad (1)$$

where  $\boldsymbol{\sigma}$  is the CAUCHY stress tensor that is a function of space  $\mathbf{s} \in \Omega$ , and a point-wise (local) constitutive law which we express as:

$$\boldsymbol{\sigma}(\mathbf{s}) = \boldsymbol{\sigma}(\nabla \mathbf{u}(\mathbf{s}); m(\mathbf{s})). \quad (2)$$

where  $\mathbf{u}(\mathbf{s})$  denotes the displacement field and  $m(\mathbf{s})$  the material parameters (e.g., Young's modulus), which generally vary in space <sup>1</sup>. We remark that most of the numerical experiments are carried out under the assumption of small displacements/deformations, in which case the stress tensor  $\boldsymbol{\sigma}$  depends on  $\mathbf{u}$  through the infinitesimal strain tensor  $\boldsymbol{\epsilon} = \frac{1}{2}(\nabla \mathbf{u} + (\nabla \mathbf{u})^T)$ . This dependence, i.e., the constitutive law above, can be linear or nonlinear.

A well-posed forward model necessitates the prescription of boundary conditions, either of DIRICHLET or NEUMANN type, which can be expressed as follows:

$$\mathbf{u} = \mathbf{f} \quad \text{on } \Gamma_D, \quad (3)$$

$$\boldsymbol{\sigma} \cdot \vec{\mathbf{n}} = \mathbf{g} \quad \text{on } \Gamma_N, \quad (4)$$

where  $\mathbf{f}$  and  $\mathbf{g}$  are given on the boundaries  $\Gamma_D$  and  $\Gamma_N$  (with  $\Gamma_D \cap \Gamma_N = \emptyset$ ,  $\Gamma_D \cup \Gamma_N = \partial\Omega$ ) and  $\vec{\mathbf{n}}$  is the outward, unit normal vector.

We emphasize that, as in all PDE-based inverse problems, the model is assumed to be correct, up at least to any discretization errors. This assumption is especially precarious given the phenomenology of constitutive laws and the variability of biological tissues. It constitutes a potential source of *model error/bias* [49] which, if present, does not prevent one from solving the inverse problem and obtaining estimates of the material parameters  $m$ , but, as it is easily understood, these estimates would be erroneous or even misleading.

We denote abstractly with  $\mathbf{u}(m)$  the displacement field arising by solving the aforementioned equations and its dependence on the material property field  $m$ . In the context of the inverse elastography problem, one is supplied with measurements  $\hat{\mathbf{u}} = \{\hat{u}_i\}_{i=1}^{N_{\hat{\mathbf{u}}}}$  of the displacements obtained usually through ultrasound or MRI at specific locations of the domain  $\Omega$ . Each such measurement  $\hat{u}_i$  is usually assumed to relate to the model-predicted displacement  $u_i(m)$  at the same point as:

$$\hat{u}_i = u_i(m) + \tau^{-0.5} \epsilon_i, \quad \epsilon_i \sim \mathcal{N}(\mathbf{0}, \mathbf{1}), \quad (5)$$

---

<sup>1</sup>In order to simplify the notation, we will omit indicating explicitly dependence on space  $\mathbf{s}$  when it is obvious from the context.

where the additive term accounts for the stochastic observation noise, which is assumed to be Gaussian distributed with variance  $\tau^{-1}$ . In the probabilistic (i.e., Bayesian) framework advocated in this work, the aforementioned equation gives rise to a likelihood  $p(\hat{\mathbf{u}}|m)$  which, when combined with a prior  $p(m)$ , gives rise to the sought posterior density  $p(m|\hat{\mathbf{u}})$ <sup>2</sup>:

$$\begin{aligned} p(m|\hat{\mathbf{u}}) &\propto p(\hat{\mathbf{u}}|m) p(m) \\ &\propto \prod_{i=1}^{N_{\hat{\mathbf{u}}}} \mathcal{N}(\hat{\mathbf{u}}_i | \mathbf{u}_i(m), \tau^{-1}) p(m). \end{aligned} \quad (6)$$

Classical inference techniques employ the PDE-solver as a black box, which implies that a solution to the PDE is required for each likelihood evaluation. Especially when the representation of the unknown field  $m$  is high-dimensional, derivatives of the (log)posterior/likelihood are required to explore the search space efficiently. This, in turn, necessitates a differentiable PDE-solver, which can be achieved using adjoint formulations [56]. This adds further complication, which, as mentioned in the introduction, creates an insurmountable modeling barrier for medical practitioners. We further note that differentiability is not available in most legacy solvers, which would preclude their use in the context of such inverse problems. We emphasize that the requirement for derivatives is also present when deterministic solutions to the inverse problem are sought [57].

### 3 Proposed method / Methodology

#### 3.1 Overview of the framework

We propose a reformulation of the inverse problem that obviates the need for a forward model while retaining the valuable information that the governing PDE provides. We view the latter as an information source, which we probe with weighted residuals. Before embarking on the presentation of the particulars, and to simplify subsequent derivations, we postulate a finite-dimensional representation of the displacement field  $\mathbf{u}$  (i.e., the state variable in the governing PDE) and the unknown material parameter field  $m$ , which takes the form:

$$m(\mathbf{x}, \mathbf{s}) = \sum_{i=1}^{d_x} x_i \eta_i^x(\mathbf{s}) \quad \text{and} \quad \mathbf{u}(\mathbf{y}, \mathbf{s}) = \sum_{i=1}^{d_y} y_i \boldsymbol{\eta}_i^y(\mathbf{s}), \quad (7)$$

where  $\eta_i^x$  and  $\boldsymbol{\eta}_i^y$  are given feature functions dependent on space and  $\mathbf{x} = \{x_i\}_{i=1}^{d_x}$ ,  $\mathbf{y} = \{y_i\}_{i=1}^{d_y}$  the corresponding coefficients, respectively. The former can be, e.g., the usual Finite Element shape functions, radial basis functions, spectral representations based on, e.g., sines/cosines, wavelets, Chebyshev polynomials [58, 53]. Their role is *not* to provide a discretization scheme for the governing PDE but merely a representation of these fields. As a result, they do not need to be associated with any, e.g., finite-element mesh as those typically employed to solve the forward problem. In general,  $d_x, d_y \gg 1$  to capture the full details. One could also employ neural networks (NNs) to represent these fields. In this case, the analogs of the  $\mathbf{x}, \mathbf{y}$  above would be the associated weights/biases.

---

<sup>2</sup>To simplify the presentation and minimize notational complexity, we have not considered at this stage the discretization of the governing PDE nor of the unknown field  $m$ . This does not imply that prior/posterior densities on spatially varying fields must be specified, which requires appropriate mathematical care.

We consider weighted residuals of the governing PDE in Equations (1)-(4) based on vector-valued weight functions  $\mathbf{w}(\mathbf{s}) \in \mathcal{W} \subset H^1(\Omega)$  such that  $\mathbf{w}|_{\Gamma_D} = 0$ . By employing integration-by-parts, one arrives at the following expression (in indicial notation) for each such weight function  $\mathbf{w}$  [59]:

$$r_{\mathbf{w}}(\mathbf{x}, \mathbf{y}) = \int_{\Omega} \sigma_{ij} w_{i,j} d\Omega - \int_{\Gamma_N} g_i w_i d\Gamma_N, \quad (8)$$

which implicitly depends on  $\mathbf{x}$  and  $\mathbf{y}$  given Equation (7) and the dependence of the stresses  $\boldsymbol{\sigma}$  on  $\mathbf{u}$  through the constitutive equation in (2). We note that depending on the choice of the weight functions  $\mathbf{w}$ , one can obtain a minimum of six methods (i.e., collocation, sub-domain, least-squares, (Petrov)-Galerkin, moments) [60]. As it will become evident, the weighted residuals serve as data sources rather than as a means to deriving a discretized system of equations as it is done conventionally. Consequently, we have the flexibility to explore alternative or even non-symmetric versions concerning  $\mathbf{u}$ ,  $\boldsymbol{\sigma}$ , or  $\mathbf{w}$ . For instance, this includes expressions involving lower-order derivatives of the candidate solution  $\mathbf{u}$ , obtained through further applications of integration by parts [61].

We consider a set of  $N$  distinct weight functions  $\mathbf{w}^{(j)}$  and corresponding weighted residuals  $r_{\mathbf{w}^{(j)}}(\mathbf{x}, \mathbf{y})$ . We assume that a *virtual* observation  $\hat{r}_j = 0$  for each residual is available, which relates to the actual residual as:

$$0 = \hat{r}_j = r_{\mathbf{w}^{(j)}}(\mathbf{y}, \mathbf{x}) + \lambda^{-1} \epsilon_j, \quad \epsilon_j \sim \mathcal{N}(0, 1) \quad (9)$$

If we denote summarily all the *virtual* observables  $\hat{\mathbf{R}} = \{\hat{r}_j = 0\}_{j=1}^N$ , the equation above gives rise to a *virtual* likelihood:

$$\begin{aligned} p(\hat{\mathbf{R}}|\mathbf{y}, \mathbf{x}) &= \prod_{j=1}^N p(\hat{r}_j = 0 | \mathbf{y}, \mathbf{x}) \\ &\propto \prod_{j=1}^N \sqrt{\lambda} \exp\left(-\frac{\lambda}{2} r_{\mathbf{w}^{(j)}}^2(\mathbf{y}, \mathbf{x})\right), \end{aligned} \quad (10)$$

where the hyper-parameter  $\lambda > 0$  penalizes the deviation of the weighted residuals from 0, i.e. the value they would attain for any solution pair  $\mathbf{x}, \mathbf{y}$  (or equivalently  $m$  and  $\mathbf{u}$ ). Selecting values for  $\lambda^{-1}$  similar to the numerical tolerance of a deterministic iterative solver has proven to be a good strategy as its role is similar in nature. We note that evaluating the *virtual* likelihood involves computing  $N$  integrals over the problem domain (see Equation (8)) as compared to the *black-box* forward solver, which classical formulations entail. The integrations over the problem domain can either be carried out deterministically or by Monte Carlo (see Appendix A).

The *virtual* likelihood above is complemented by the actual likelihood of the displacement observations  $\hat{\mathbf{u}}$ . In particular, by evaluating the displacement field in Equation (7) at the locations where displacements are provided, we obtain  $u_i(\mathbf{y})$  which as in Equation (6) give rise to the *actual* likelihood:

$$\begin{aligned} p(\hat{\mathbf{u}}|\mathbf{y}) &= \prod_{i=1}^{N_{\hat{\mathbf{u}}}} \mathcal{N}(\hat{u}_i | u_i(\mathbf{y}), \tau^{-1}) \\ &\propto \prod_{i=1}^{N_{\hat{\mathbf{u}}}} \sqrt{\tau} e^{-\frac{\tau}{2} (\hat{u}_i - u_i(\mathbf{y}))^2} \end{aligned} \quad (11)$$

A mere application of Bayes rule would then yield the following *joint posterior* on  $\mathbf{x}$  and  $\mathbf{y}$ :

$$p(\mathbf{x}, \mathbf{y} | \hat{\mathbf{R}}, \hat{\mathbf{u}}) = \frac{p(\hat{\mathbf{u}}|\mathbf{y}) p(\hat{\mathbf{R}}|\mathbf{y}, \mathbf{x}) p(\mathbf{y}, \mathbf{x})}{p(\hat{\mathbf{R}}, \hat{\mathbf{u}})} \quad (12)$$

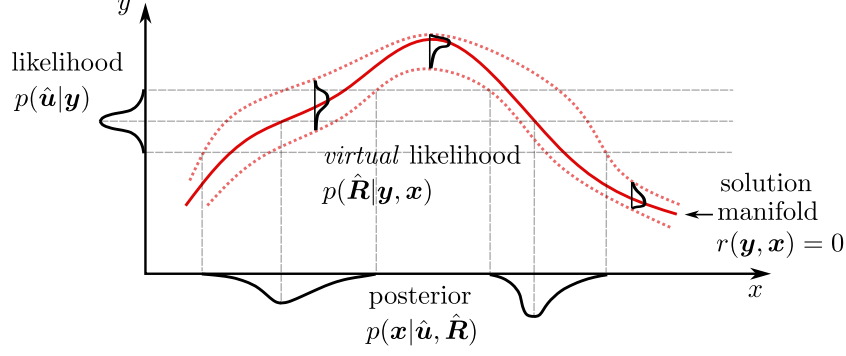


Figure 1: Schematic illustration of the proposed formulation. The actual data  $\hat{\mathbf{u}}$  induces an actual likelihood  $p(\hat{\mathbf{u}}|\mathbf{y})$  on the (representation of the) PDE-solution  $\mathbf{y}$ . This is combined with the *virtual* likelihood  $p(\hat{\mathbf{R}}|\mathbf{y}, \mathbf{x})$  that assigns probabilities to  $(\mathbf{x}, \mathbf{y})$  pairs. The virtual likelihood is highest on the solution manifold, i.e., for all  $(\mathbf{x}, \mathbf{y})$  pairs that yield 0 values for the weighted residuals  $r(\mathbf{y}, \mathbf{x})$  and decays at a rate determined by the precision  $\lambda$  as one moves away from it. The combination of these two likelihoods (and the priors which are not depicted here) gives rise to the sought posterior  $p(\mathbf{x}|\hat{\mathbf{u}}, \hat{\mathbf{R}})$  on (the representation of) the unknown material field  $\mathbf{x}$ .

where  $p(\mathbf{y}, \mathbf{x})$  denotes the prior and  $p(\hat{\mathbf{R}}, \hat{\mathbf{u}})$  the model evidence. With regards to the former, in subsequent numerical illustrations, we employ the following form:

$$p(\mathbf{y}, \mathbf{x}) = p(\mathbf{y})p(\mathbf{x}), \quad (13)$$

where  $p(\mathbf{x})$  may be the same prior as in a traditional formulation. A vague, uninformative prior was employed for  $p(\mathbf{y})$ , reflecting prior beliefs about the PDE solution as represented by  $\mathbf{y}$ . Naturally, other forms could be employed, including hyper-parameters, which could be fine-tuned during inference it is done in [53]. In our formulation however, the role of  $p(\mathbf{x}, \mathbf{y})$  is not to provide accurate predictions of the forward or backward map between  $\mathbf{y}$  and  $\mathbf{x}$ , as this is the purpose of the posterior, which is discussed in the subsequent section.

### Remarks

- In contrast to classical Bayesian formulations, our sought posterior is defined jointly on  $\mathbf{x}$  and  $\mathbf{y}$ , which must both be inferred. The increased dimension of the state space allows us to circumvent the black-box solver. In fact, the formulation and solution of the inverse problem **does not require the availability of a forward model or even a well-posed forward problem**. As we show in the sequel, the form of the terms involved on the right-hand side of Equation (12) enables fast inference despite the increased dimension.
- The posterior obtained will depend on the virtual observables  $\hat{\mathbf{R}}$  employed both in terms of their number  $N$  as well as in terms of the weight functions these are based on. In general, the higher the  $N$ , the more information from the PDE is incorporated and the closer one would be to the solution manifold that consists of all pairs of  $\mathbf{x}$  and  $\mathbf{y}$  that yield 0 residuals, i.e., they are solution pairs of the PDE (Figure 1).



### 3.2 Probabilistic Inference and randomization of residuals

The exact posterior in Equation (12) is generally intractable. For that purpose, we advocate the use of Variational Inference, i.e., we seek an approximation from a parametrized family of densities  $q_{\xi}(\mathbf{x}, \mathbf{y})$  by minimizing the KULLBACK-LEIBLER (KL) divergence with the exact posterior. If  $\xi$  denotes the tunable parameters, then this is equivalent to maximizing the Evidence Lower BOund (ELBO)  $\mathcal{L}(\xi)$  to the log-evidence  $\log p(\hat{\mathbf{R}}, \hat{\mathbf{u}})$  [21]:

$$\begin{aligned}
 \log p(\hat{\mathbf{R}}, \hat{\mathbf{u}}) &= \log \int p(\hat{\mathbf{u}}|\mathbf{y})p(\hat{\mathbf{R}}|\mathbf{y}, \mathbf{x})p(\mathbf{y}, \mathbf{x})d\mathbf{y}d\mathbf{x} \\
 &\geq \left\langle \log \frac{p(\hat{\mathbf{u}}|\mathbf{y})p(\hat{\mathbf{R}}|\mathbf{y}, \mathbf{x})p(\mathbf{y}, \mathbf{x})}{q_{\xi}(\mathbf{y}, \mathbf{x})} \right\rangle_{q_{\xi}(\mathbf{y}, \mathbf{x})} \\
 &= -\frac{\lambda}{2} \sum_{j=1}^N \langle r_{\mathbf{w}^{(j)}}^2(\mathbf{y}, \mathbf{x}) \rangle_{q_{\xi}(\mathbf{y}, \mathbf{x})} - \frac{\tau}{2} \sum_{i=1}^{N_{\hat{\mathbf{u}}}} \langle (\hat{u}_i - u_i(\mathbf{y}))^2 \rangle_{q_{\xi}(\mathbf{y}, \mathbf{x})} \\
 &\quad + \left\langle \log \frac{p(\mathbf{y}, \mathbf{x})}{q_{\xi}(\mathbf{y}, \mathbf{x})} \right\rangle_{q_{\xi}(\mathbf{y}, \mathbf{x})} \\
 &= \mathcal{L}(\xi),
 \end{aligned} \tag{14}$$

where  $\langle \cdot \rangle_{q_{\xi}}$  denotes the expectation with respect to  $q_{\xi}$ . The first term of the ELBO promotes the (on average) minimization of the  $N$  weighted residuals, the second minimizes (on average) the discrepancy between model predictions and the measurements, whereas the third provides a regularization by minimizing the KL-divergence with the prior. We note the resemblance of the ELBO with alternative formulations that have been proposed, such as PINNs [42] or weak adversarial networks [43]. Generally, these employed ad-hoc coefficients as relative weights for the aforementioned terms and made use of collocation-type residuals, which arise as a special case in our formulation (i.e., by using Dirac-deltas as the weight functions). More importantly, however, our formulation enables a fully probabilistic interpretation in which the information content of the weighted residuals can be quantified, as discussed in the sequel.

In Equation (14), it is evident that maximizing the ELBO requires repeated evaluations of the  $N$  weighted residuals (as well as their derivatives with respect to the parameters  $\xi$ ). As mentioned earlier, the higher the  $N$  is, the more information from the governing PDE is incorporated, but the higher the computational cost becomes. To improve the efficiency of this computation, we advocate a Monte Carlo approximation for the first term in Equation (14), i.e.:

$$\sum_{j=1}^N \langle r_{\mathbf{w}^{(j)}}^2(\mathbf{y}, \mathbf{x}) \rangle_{q_{\xi}(\mathbf{y}, \mathbf{x})} \approx \frac{N}{K} \sum_{k=1}^K \langle r_{\mathbf{w}^{(j_k)}}^2(\mathbf{y}, \mathbf{x}) \rangle_{q_{\xi}(\mathbf{y}, \mathbf{x})}, \quad j_k \sim \text{Cat}\left(N, \frac{1}{N}\right). \tag{15}$$

Thus, we randomly sample  $K \ll N$  weight functions and the corresponding  $K$  weighted residuals provide an unbiased Monte Carlo estimator of this ELBO term even for  $K = 1$ .

In section 3.4 and in greater detail in Appendix Appendix B, we explain how to compute the gradients of  $\mathcal{L}$  and use them for its maximization. We also note that if a parameterized prior, e.g.  $p_{\zeta}(\mathbf{x}, \mathbf{y})$  were used, the optimal  $\zeta$  can be found by maximizing the resulting ELBO [52]. While these structured or informative priors could greatly improve inference speed and prediction accuracy, this paper does not explore their potential.

We finally note that the ELBO provides a quantitative metric of the information content of each weighted residual. As a result, and rather than randomly sub-sampling residuals, one could envision procedures that could lead to selecting weighting functions of superior informational content, which

are not explored in this paper. Another possibility could be to localize weight functions in regions of the problem domain where inferential uncertainty is higher or which are of increased interest to the analyst. Similar to the way one can zoom in on a photo, the framework advocated employs weight functions as indirect magnifying glasses that enable one to zoom in on the underlying and unobserved material property field.

### 3.3 Approximate posterior $q_\xi$

The form of the approximate posterior  $q_\xi$  plays a crucial role in the efficacy and accuracy of the formulation. It has to be expressive enough to approximate the actual posterior and as simple as possible to increase computational efficiency and interpretability. It is clear that  $\mathbf{x}$  and  $\mathbf{y}$  are strongly dependent as they must jointly ensure that the weighted residuals in the virtual likelihood are in the vicinity of zero. Capturing this dependence is crucial to properly quantifying the uncertainty in  $\mathbf{x}$ , i.e., the representation of the material property field  $m$ . To this end we factorize the joint, approximate posterior  $q_\xi$  as follows:

$$q_\xi(\mathbf{x}, \mathbf{y}) = q_\xi(\mathbf{x}|\mathbf{y}) q_\xi(\mathbf{y}) \quad (16)$$

The first of these densities takes the form:

$$q_\xi(\mathbf{x}|\mathbf{y}) = \mathcal{N}(\mathbf{x} | \boldsymbol{\mu}_{\mathbf{x};\xi_{\mathbf{x}}}(\mathbf{y}), \mathbf{S}_{\mathbf{x}}), \quad (17)$$

where the conditional mean  $\boldsymbol{\mu}_{\mathbf{x}}$  is parametrized by a neural network with tunable parameters  $\xi_{\mathbf{x}}$ , the details of which are contained in Appendix C. The conditional covariance  $\mathbf{S}_{\mathbf{x}}$  is assumed to be independent of  $\mathbf{y}$  and of the form:

$$\mathbf{S}_{\mathbf{x}} = \mathbf{L}_{\mathbf{x}}\mathbf{L}_{\mathbf{x}}^T + \text{diag}(\boldsymbol{\sigma}_{\mathbf{x}}^2) \quad (18)$$

where  $\mathbf{L}_{\mathbf{x}}$  is a matrix of dimension  $d_{\mathbf{x}} \times d_{\tilde{\mathbf{x}}}$  that captures the principal directions along which (conditional) variance is larger whereas  $\boldsymbol{\sigma}_{\mathbf{x}}^2$  is a vector of dimension  $d_{\mathbf{x}}$  that captures the residual (conditional) variance along the  $\mathbf{x}$ - dimensions. In contrast to a full covariance matrix, the form adopted for  $\mathbf{S}_{\mathbf{x}}$  ensures linear scaling of the unknown parameters with  $d_{\mathbf{x}}$ , which for most problems can be high.

With regards to the second density in Equation (16), we adopt the following form:

$$q_\xi(\mathbf{y}) = \mathcal{N}(\mathbf{y} | \boldsymbol{\mu}_{\mathbf{y}}, \mathbf{S}_{\mathbf{y}}) \quad (19)$$

where again a similar form for  $\mathbf{S}_{\mathbf{y}}$  is adopted in order to ensure linear scaling with  $d_{\mathbf{y}}$ , i.e.:

$$\mathbf{S}_{\mathbf{y}} = \mathbf{L}_{\mathbf{y}}\mathbf{L}_{\mathbf{y}}^T + \text{diag}(\boldsymbol{\sigma}_{\mathbf{y}}^2), \quad (20)$$

where  $\mathbf{L}_{\mathbf{y}}$  is rectangular matrix of dimensions  $d_{\mathbf{y}} \times d_{\tilde{\mathbf{y}}}$  (where  $d_{\tilde{\mathbf{y}}} \ll d_{\mathbf{y}}$ ) and  $\boldsymbol{\sigma}_{\mathbf{y}}^2$  is a vector of dimensions  $d_{\mathbf{y}}$ . As a result the vector of parameters  $\xi$  that are optimized in order to maximize the ELBO  $\mathcal{L}(\xi)$  consists of:

$$\xi = \{\xi_{\mathbf{x}}, \mathbf{L}_{\mathbf{x}}, \boldsymbol{\sigma}_{\mathbf{x}}^2, \boldsymbol{\mu}_{\mathbf{y}}, \mathbf{L}_{\mathbf{y}}, \boldsymbol{\sigma}_{\mathbf{y}}^2\} \quad (21)$$

---

**Algorithm 1** SVI Training Algorithm

---

Select  $\lambda, \tau, K, L$ ; Initialize  $\xi \leftarrow \xi_0, t \leftarrow 0$   
**while**  $\mathcal{L}$  not converged **do**  
  Generate  $K$  weight functions  $w^{(jk)}$   
  **for**  $\ell = 1$  to  $L$  **do**  
    Draw  $\mathbf{y}_\ell \leftarrow \boldsymbol{\mu}_y + \mathbf{L}_y \boldsymbol{\varepsilon}_1 + \boldsymbol{\sigma}_y \boldsymbol{\varepsilon}_2, \boldsymbol{\varepsilon}_1 \sim \mathcal{N}(\mathbf{0}, \mathbf{I}_{d_{\bar{y}}}), \boldsymbol{\varepsilon}_2 \sim \mathcal{N}(\mathbf{0}, \mathbf{I}_{d_y})$   
     $\boldsymbol{\mu}_{n,x} \leftarrow NN(\mathbf{y}_\ell)$  ▷ see Equation (17)  
    Draw  $\mathbf{x}_\ell \leftarrow \boldsymbol{\mu}_{x;\xi_x}(\mathbf{y}_\ell) + \mathbf{L}_x \boldsymbol{\varepsilon}_3 + \boldsymbol{\sigma}_x \boldsymbol{\varepsilon}_4, \boldsymbol{\varepsilon}_3 \sim \mathcal{N}(\mathbf{0}, \mathbf{I}_{d_{\bar{x}}}), \boldsymbol{\varepsilon}_4 \sim \mathcal{N}(\mathbf{0}, \mathbf{I}_{d_x})$   
  **end for**  
  Estimate  $\mathcal{L}_\xi(\mathbf{x}_\ell, \mathbf{y}_\ell, w^{(jk)})$  ▷ see Equation (36)  
  Estimate  $\nabla_\xi \mathcal{L}_\xi$  ▷ see Appendix B  
  Update  $\xi_{t+1} \leftarrow \xi_t + \boldsymbol{\rho}^{(t)} \odot \nabla_\xi \mathcal{L}_\xi$  ▷ Step sizes  $\boldsymbol{\rho}$  via ADAM  
   $t \leftarrow t + 1$   
**end while**

---

and is of dimension  $dim(\xi_x) + d_x \times (d_{\bar{x}} + 1) + d_y \times (d_{\bar{y}} + 2)$ . Algorithmic details about the maximization of the ELBO are contained in section 3.4. In section 3.5, we describe how the density  $q_\xi$  can be used to obtain probabilistic estimates of the unknown material property field  $m$ .

### 3.4 Stochastic Variational Inference for the maximization of the ELBO

The maximization of the ELBO  $L(\xi)$  is carried out in the context of Stochastic Variational Inference [62], which is based on Monte Carlo estimates of  $L(\xi)$  and its gradient in conjunction with Stochastic Gradient Ascent for the maximization. Regarding the former, we use the reparameterization trick [63] to generate samples from the approximate posterior  $q_\xi$ . Based on the form of  $q_\xi$  discussed in the previous section, this can be done by drawing first  $\mathbf{y}$ -samples from  $q_\xi(\mathbf{y})$  (Equation (19)) as:

$$\mathbf{y} = \boldsymbol{\mu}_y + \mathbf{L}_y \boldsymbol{\varepsilon}_1 + \boldsymbol{\sigma}_y \odot \boldsymbol{\varepsilon}_2, \quad \boldsymbol{\varepsilon}_1 \sim \mathcal{N}(\mathbf{0}, \mathbf{I}_{d_{\bar{y}}}) \text{ and } \boldsymbol{\varepsilon}_2 \sim \mathcal{N}(\mathbf{0}, \mathbf{I}_{d_y}) \quad (22)$$

and in a second step using them to sample  $\mathbf{x}$  from the conditional posterior  $q_\xi(\mathbf{x}|\mathbf{y})$  (Equation (17)) as:

$$\mathbf{x} = \boldsymbol{\mu}_{x;\xi_x}(\mathbf{y}) + \mathbf{L}_x \boldsymbol{\varepsilon}_3 + \boldsymbol{\sigma}_x \odot \boldsymbol{\varepsilon}_4, \quad \boldsymbol{\varepsilon}_3 \sim \mathcal{N}(\mathbf{0}, \mathbf{I}_{d_{\bar{x}}}) \text{ and } \boldsymbol{\varepsilon}_4 \sim \mathcal{N}(\mathbf{0}, \mathbf{I}_{d_x}) \quad (23)$$

where  $\boldsymbol{\mu}_{x;\xi_x}(\cdot)$  denotes the neural network described in Appendix C. We generate  $L$  such sample pairs  $(\mathbf{x}, \mathbf{y})$  which are used to produce Monte Carlo estimates of the expectations with respect to  $q_\xi$  appearing in the ELBO (Equation (14)) and its gradient, which is computed via PyTorch's automatic differentiation capability [64]. Detailed expressions can be found in Appendix B, and a pseudo-code is shown in Algorithm 1.

### 3.5 Probabilistic estimates of unknown material property field

After convergence of the SVI scheme and upon identification of the optimal values for  $\xi$ , probabilistic estimates of the unknown material property field  $m(s)$  through the approximate posterior  $q_\xi(\mathbf{y}, \mathbf{x})$ . In particular, posterior predictive samples  $m_b(s)$  of the material property field at arbitrary locations  $s \in \Omega$  can be obtained by drawing samples, say  $\mathbf{x}_b$ , from  $q_\xi(\mathbf{y}, \mathbf{x})$  and combining them with the feature functions in Equation (7) in order to obtain samples, say  $m_b(s)$  of the sought material property field. Such samples can be generated as described in Equations (22), (23) earlier. Estimates of the

---

**Algorithm 2** Material field  $m(\mathbf{s})$  posterior estimates

---

```
Select  $B$                                 ▷ Number of samples
for  $b$  in  $B$  do
   $\mathbf{y}_b \sim q_\xi(\mathbf{y} | \boldsymbol{\mu}_y, \mathbf{S}_y)$       ▷ see Equation (22)
   $\boldsymbol{\mu}_{b,x} \leftarrow NN(\mathbf{y}_b)$ 
   $\mathbf{x}_b \sim q(\boldsymbol{\mu}_{b,x}, \mathbf{S}_x)$         ▷ see Equation (23)
   $m_b(\mathbf{s}) \leftarrow \sum \mathbf{x}_b \boldsymbol{\eta}^x(\mathbf{s})$   ▷ see Equation (7)
end for
Estimate  $\mathbb{E}[m(\mathbf{s}) | \hat{\mathbf{u}}, \hat{\mathbf{R}}]$ ,  $Var[m(\mathbf{s}) | \hat{\mathbf{u}}, \hat{\mathbf{R}}]$   ▷ see Equation (24) / Equation (25)
 $Q_{0.025}(m(\mathbf{s})) \leftarrow \text{quantile}(m_b(\mathbf{s}), 0.025)$   ▷ see Equation (26)
 $Q_{0.975}(m(\mathbf{s})) \leftarrow \text{quantile}(m_b(\mathbf{s}), 0.975)$   ▷ see Equation (27)
```

---

posterior mean  $\mathbb{E}[m(\mathbf{s}) | \hat{\mathbf{u}}, \hat{\mathbf{R}}]$  and variance  $Var[m(\mathbf{s}) | \hat{\mathbf{u}}, \hat{\mathbf{R}}]$  can be obtained as follows:

$$\mathbb{E}[m(\mathbf{s}) | \hat{\mathbf{u}}, \hat{\mathbf{R}}] = \frac{1}{B} \sum_{b=1}^B m_b(\mathbf{s}) \quad \text{and} \quad (24)$$

$$Var[m(\mathbf{s}) | \hat{\mathbf{u}}, \hat{\mathbf{R}}] = \frac{1}{B} \sum_{b=1}^B (m_b(\mathbf{s}) - \hat{m}(\mathbf{s}))^2. \quad (25)$$

Furthermore, we report in the subsequent numerical illustrations 95% credible intervals which are obtained with the help of 2.5% and 97.5% posterior quantiles at each spatial location  $\mathbf{s} \in \Omega$ :

$$Q_{0.025}(m(\mathbf{s})) = \text{quantile}(m_b(\mathbf{s}), 0.025) \quad \text{and} \quad (26)$$

$$Q_{0.975}(m(\mathbf{s})) = \text{quantile}(m_b(\mathbf{s}), 0.975), \quad (27)$$

respectively. The illustrations contained in section 4 were based on  $B = 1000$  posterior samples. An algorithmic summary of the steps described above can be found in Algorithm 2.

## 4 Numerical Illustrations

In this section, we showcase the effectiveness of our approach on two-dimensional problems employing synthetic displacement data for high-dimensional linear and nonlinear PDEs. Our objectives are:

- to compare in terms of accuracy and efficiency with classical inference schemes such as Hamiltonian Monte Carlo (HMC, [65]) and Stochastic Variational Inference (SVI, [62]) that employ the forward solver as a black-box for the solution of the Bayesian inverse problem (section 4.2).
- to demonstrate the proposed method's capability to produce accurate results in the presence of various noise levels (section 4.3),
- to highlight its ability to produce solutions to problems for which a well-posed, forward model is unavailable, as is the case when essential boundary conditions are not prescribed (section 4.4),

- to elucidate the proposed method’s ability to handle seamlessly linear and nonlinear problems (section 4.5) with no alterations in the algorithmic framework and without any noticeable computational overhead.

#### 4.1 Problem setup and implementation details

The experimental setup (Figure 3) is motivated by applications in elastography, where we want to identify inclusions (e.g., tumors) in healthy tissue. The governing equations of small-strain, solid mechanics described in Equations (1), (2) were employed for the square domain  $\Omega = [0, 1]^2$  and for the boundary conditions shown in Figure 3. The constitutive laws employed are described in the subsequent sections. Reference solutions of the forward problem were obtained with FEniCS [66, 67] using a triangular mesh with a total of 15,625 nodal points. The displacements on  $\hat{\mathbf{u}}_{ref} = \{u_{i,ref}\}_{i=1}^{N_{\hat{\mathbf{u}}}}$  on a regular  $32 \times 32$  grid were subsequently contaminated with additive Gaussian noise with variance  $\tau^{-1}$  in order to produce synthetic data  $\hat{\mathbf{u}}$  used for the solution of the inverse problem. We report the noise variance  $\tau^{-1}$  in terms of the Signal-to-Noise (SNR) ratio defined as:

$$SNR_{dB} = 10 \cdot \log_{10} \sqrt{\tau \frac{1}{N_{\hat{\mathbf{u}}}} \sum_{i=0}^{N_{\hat{\mathbf{u}}}} u_{i,ref}^2}, \quad (28)$$

which, unless otherwise mentioned, it is taken equal to 30 dB. We note that higher SNR means less noise and vice versa.

The black-box forward solver employed for the solution of the Bayesian inverse problem using classical inference techniques was based on FEniCS [66] with a regular mesh consisting of triangles as described in the sequel. The derivatives were obtained via PyAdjoint [68].

For the solution of the inverse problem using the proposed method, we employed feature functions associated with the aforementioned uniform, triangular mesh over the problem domain. In particular, the  $\eta_i^x$  used in Equation (7) to represent the property field  $m$  were piece-wise constant over each triangular element resulting in  $dim(\mathbf{x}) = d_x = 1922$ . The feature functions  $\eta_i^y$  used in Equation (7) to represent the displacement field  $\mathbf{u}$  were taken to be the usual FE shape functions (i.e. piece-wise linear) associated with this triangular mesh resulting in  $dim(\mathbf{y}) = d_y = 2048$ . While many other possibilities exist, as discussed earlier, the advantage of the representation adopted for  $m$  is that the entries of  $\mathbf{x}$  are associated with each triangular element’s center point. As a result, one can introduce structured, spatial priors on  $\mathbf{x}$  as explained in the sequel.

The weight functions  $\mathbf{w}(\mathbf{s})$  employed in the weighted residuals, were expressed with the same shape functions as  $\mathbf{u}$  as follows:

$$\mathbf{w}(\mathbf{z}, \mathbf{s}) = \sum_{i=1}^{d_y} z_i \eta_i^y(\mathbf{s}). \quad (29)$$

Since each  $\eta_i^y(\mathbf{s})$ , and therefore  $z_i$ , is associated with a nodal point of the aforementioned triangular mesh, we generated  $N = 24,576$  such weight functions  $\mathbf{w}^{(j)}$  (from which  $K$  were subsampled at each iteration of Algorithm 1), by drawing circles at uniformly sampled nodal locations and with random radii uniformly sampled in the interval  $[0, 0.15]$ . Subsequently, all the  $z_i$  associated with

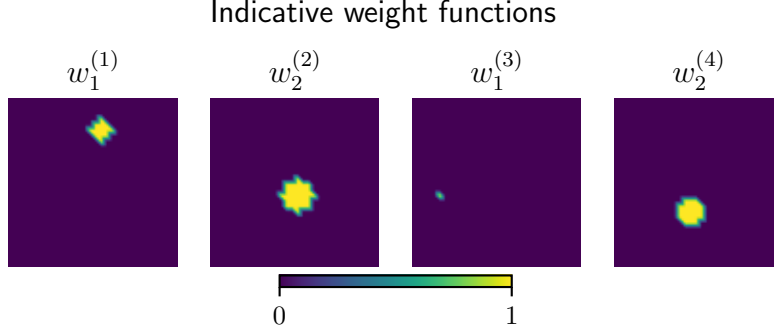


Figure 2: Illustration of 4 randomly selected weight functions  $\mathbf{w}^{(j)}$  used in the algorithm. Note that for each weight function depicted are only the dimensions  $w_1^{(j)}$  or  $w_2^{(j)}$  which have non-zero values.

nodal points falling within the circle were set equal to 1, and the rest were equal to 0. Figure 2 depicts some indicative weight functions.

An independent prior  $p(\mathbf{x}, \mathbf{y}) = p(\mathbf{y})p(\mathbf{x})$  was employed. For the representation of the displacement field i.e.  $\mathbf{y}$  an uninformative, zero-mean, Gaussian prior with isotropic variance  $10^{16}$  was employed i.e.  $p(\mathbf{y}) = \mathcal{N}(\mathbf{y} | \mathbf{0}, 10^{16}\mathbf{I})$ . For the representation of the unknown material property field, i.e.,  $\mathbf{x}$ , a prior suitable for identifying inclusions was employed [69]. In particular, we denote with  $\mathbf{J}_x = \mathbf{B} \mathbf{x}$  the vector of jumps between neighboring points of dimension  $d_{jumps}$ . We imposed a hierarchical prior on  $\mathbf{J}_x$  that consists of:

$$\begin{aligned} p(\mathbf{x}|\boldsymbol{\theta}) &= \mathcal{N}(\mathbf{J}_x | \mathbf{0}, \text{diag}(\boldsymbol{\theta}^{-1})) \\ p(\boldsymbol{\theta}) &= \prod_{j=1}^{d_{jumps}} \text{Gamma}(\theta_j | a_0, b_0) \end{aligned} \quad (30)$$

The precision hyper-parameters  $\boldsymbol{\theta}$  promote sparsity in the number of jumps, i.e., piece-wise constant solutions [69]. Posed differently, amongst candidate solutions  $\mathbf{x}$ , which fit the data equally well, the ones with the least total magnitude of the jumps between neighboring points are preferred. The values  $a_0 = b_0 = 10^{-8}$  were used in subsequent simulations [70]. Inference of the associated hyper-parameters  $\boldsymbol{\theta}$  is discussed in Appendix D and implies a negligible additional computational cost.

With regards to the approximate posterior  $q_{\xi}(\mathbf{x}, \mathbf{y})$  described in subsection 3.3 the following parameter values were employed  $\dim(\boldsymbol{\xi}_x) = 15,946,000$  and  $d_{\bar{\mathbf{x}}} = d_{\bar{\mathbf{y}}} = 10$  which resulted in an overall dimension of the parameter vector  $\mathbf{x}^{(i)}$  of  $\dim(\boldsymbol{\xi}) = 15,991,718$ . The parameters  $\boldsymbol{\xi}_x$  correspond to a fully connected neural network with 3 hidden layers and 2000 neurons appearing in Equation (17).

With regards to implementation details for the stochastic gradient ascent, we employed ADAM [71] with  $\{\beta_1, \beta_2, lr\} = \{0.9, 0.99, 10^{-4}\}$ . We employed  $K = 200$  (Algorithm 1) weight functions per iteration as described in subsection 3.2 and  $L = 10$  samples of  $(\mathbf{x}, \mathbf{y})$  pairs from the approximate posterior for the associated Monte Carlo estimators (see Equation (36)). We found that increased efficiency can be achieved if one first updated  $q_{\xi}(\mathbf{y})$  separately on the observation data while not activating the virtual likelihood (which is equivalent to setting  $\lambda = 0$  in Equation (14)). We then train the joint approximate posterior until convergence with  $\lambda = 10^7$ . Our method was implemented in PyTorch [64] and training was carried out on an Nvidia RTX 4090 GPU. The code can be found

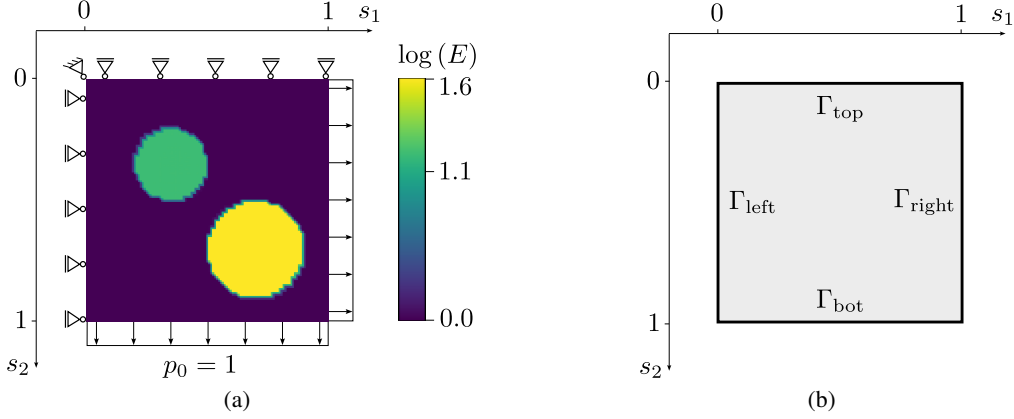


Figure 3: (a): Problem configuration with DIRICHLET BCs on boundaries  $\Gamma_{\text{top}}$  and  $\Gamma_{\text{left}}$  and NEUMANN BCs on boundaries  $\Gamma_{\text{bot}}$  and  $\Gamma_{\text{right}}$ , respectively. The domain shows the ground truth material property field  $m$  (e.g., the logarithm of YOUNG's modulus) with two circular inclusions. (b): Boundary notation convention.

on the following repository upon publication <https://github.com/pkmtum/Weak-Neural-Variational-Inference>.

## 4.2 Accuracy and Efficiency comparison

In this section, we assess the proposed method against classical Bayesian inversion techniques that use the forward solver (and its adjoint for derivatives) as a black box. The computational cost of our method is proportional to the number of weighted residual (and their gradient) evaluations. In order to make a fair comparison, we assume a first-order iterative solver is employed for the black-box version, which also relies on repeated evaluations of the weighted residuals and their derivatives. We note that each full update of such a solver requires computing all weighted residuals, whereas in our method  $K$ , such residuals are used for each SVI update. Naturally, the total number of iterations in the former case would depend on the initial guess (which itself can be dependent on the inference scheme adopted) for the solution as well as the particulars of the update equations. We discuss these aspects in detail in Appendix E where an equivalent cost in terms of weighted residual evaluations is established. We finally note that we did not use wall-clock time as a cost metric as it depends on the software/implementation (vectorization, jit, parallelization) in relation to the available hardware (CPU / GPU).

We assume first a linear, elastic constitutive law with Poisson's ratio  $\nu = 0.45$  and spatially variable Young's modulus  $m$  given by (see Figure 3):

$$\ln(m) = \begin{cases} 1.6 & \text{if } (s_1 - 0.7)^2 + (s_2 - 0.7)^2 < 0.2^2 \\ 1.1 & \text{if } (s_1 - 0.35)^2 + (s_2 - 0.35)^2 < 0.15^2 \\ 0 & \text{else.} \end{cases} \quad (31)$$

The value selected for the first inclusion is based on evidence that breast cancer tissue is approximately 5 times stiffer than normal breast tissue [72, 73, 74, 75, 76] whereas for the second inclusion on the stiffness of a liver tumor being 3 times higher compared to healthy liver tissue [75, 76].

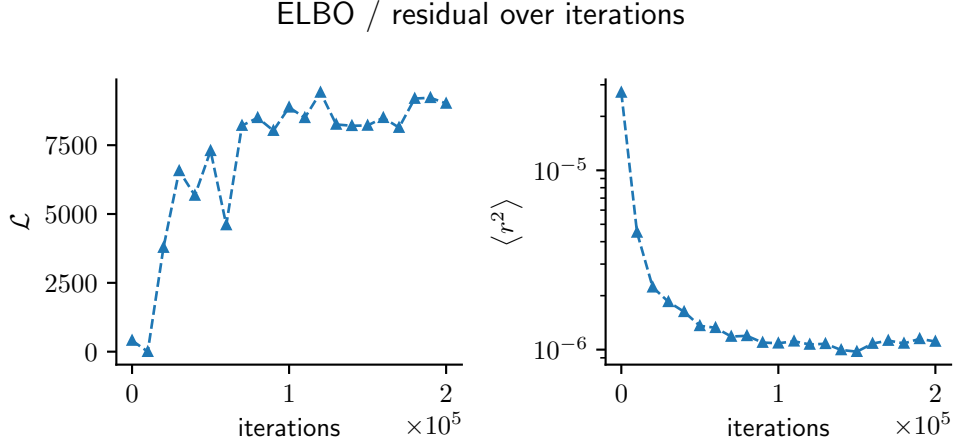


Figure 4: Convergence of the proposed method. Depicted is the change of the ELBO  $\mathcal{L}$  (left) and the expected squared residual  $\langle r^2 \rangle$  (right) over the iterations. The expected residuals are calculated using 50  $\mathbf{x}$ - $\mathbf{y}$  samples and all weight functions. The fluctuations are due to the Monte Carlo estimates employed at each iteration.

For the efficiency comparison only, we replace the jump prior in Equation (30) with a simple GAUSSIAN prior

$$p(\mathbf{x}) = \mathcal{N}(\mathbf{x} | \mu = 0, \sigma = 2), \quad (32)$$

to ensure that we compare the (general) performance of the methods, not their ability to handle a specific prior.

The convergence of our method can be observed in Figure 4, where the (rescaled) ELBO (left) and the expected square residual (right) over the iterations are depicted. In Figure 5, we depict one-dimensional cross-sections along the diagonal  $s_1 = s_2$  of the problem domain  $\Omega$  of the inferred material field obtained using HMC, SVI, and the proposed method. The top row shows the ground truth posterior obtained by an HMC run with an equivalent cost of  $1.35 \times 10^{11}$  residual evaluations (300,000 black-box forward solves). In contrast, our method (second row) converges to a posterior of similar quality after  $4 \times 10^8$  weighted residual evaluations (i.e. approximately 3 orders of magnitude less). The slightly higher posterior uncertainty of our method could be attributed to the biased approximation of the posterior and the additional noise introduced by the virtual likelihood. For the same computational cost that it took for our method to converge, the black-box-solver-based HMC (third row) and SVI (fourth row) inference schemes produce estimates that deviate significantly from the ground truth (top row). These indicative plots showcase the superior efficiency of the proposed method as compared to traditional, black-box-based ones.

### 4.3 Varying noise levels

This subsection demonstrates the proposed method’s performance under varying noise levels. In particular, we consider a linear elastic constitutive law with a spatially varying Young’s modulus as in Equation (31). We consider three noise levels  $SNR = \{25 \text{ dB}, 30 \text{ dB}, 35 \text{ dB}\}$ , defined as in Equation (28). Note that the higher the SNR is, the less noise is present in the data.



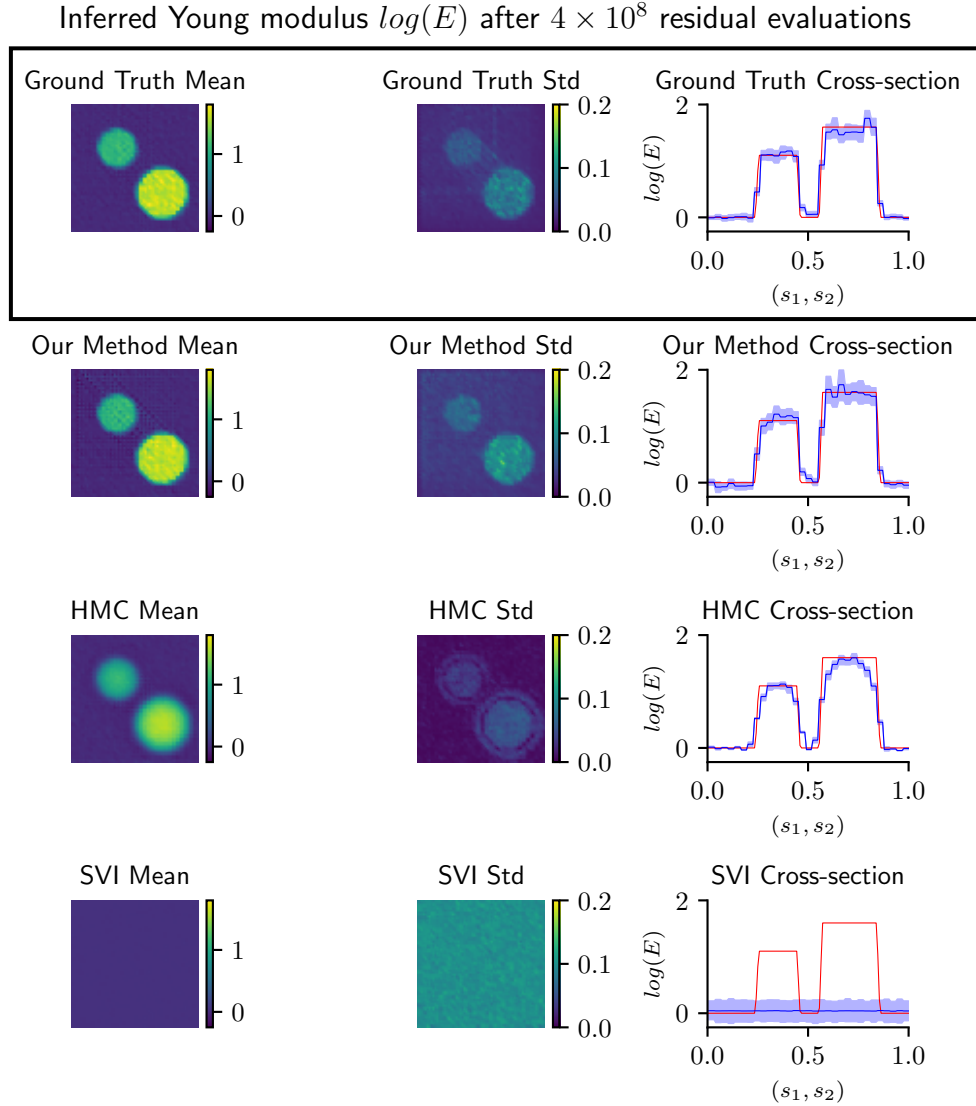


Figure 5: The three columns contain posterior mean (first), posterior standard deviation (second) over the whole domain, and posterior estimates along the diagonal  $s_1 = s_2$  of the problem domain (i.e. posterior mean  $\mu$  (blue line) and 95% credible intervals (blue shaded areas)). The first row pertains to the ground truth posterior obtained by black-box HMC run ( $1.35 \times 10^{11}$  residual evaluations). The second row corresponds to the posterior obtained by the proposed method after  $4 \times 10^8$  weighted residual evaluations. The third and fourth rows contain posterior estimates obtained with black-box HMC / SVI, respectively, and after the same number of residual evaluations as the proposed method. The results were obtained with the same synthetic data contaminated by noise with  $SNR = 30$  dB.

Figures 6 and 7 show the posterior mean and variance of the inferred displacement field (obtained through  $\mathbf{y}$ ) for  $SNR = \{25 \text{ dB}, 30 \text{ dB}, 35 \text{ dB}\}$ , respectively. While the predicted means of the displacement fields  $\mathbf{u}$  are nearly identical for all noise levels, their standard deviations increase with decreasing  $SNR$  as one would expect. The inferred material field  $m$  (obtained through  $\mathbf{x}$ ) and for

the three SNRs is shown in Figure 8. The respective posterior means are almost identical and very close to the ground truth (Figure 3), while as one would expect, the posterior variance increases when more noise is present in the data, i.e., for lower  $SNR$ . Furthermore, we notice that with increasing noise, the mean of the inclusions appears less homogeneous, and the edges are more diffuse. This is more clearly observed in the third column, which depicts posterior estimates along the diagonal  $s_1 = s_2$  of the problem domain  $\Omega$ . Nevertheless, we note that the credible intervals largely envelop the ground truth.

#### 4.4 Without Dirichlet boundary conditions

As mentioned earlier, a necessary condition of traditional solution strategies for inverse problems is the availability of a well-posed forward problem and associated numerical solver. This has obfuscated the use of model-based elastography in clinical practice as the development of such solvers, apart from cost, requires particular knowledge and modeling skills. In this section, we aim to show that the proposed framework can produce accurate inverse problem solutions without such a well-posed forward problem as would be the case when DIRICHLET boundary conditions on  $\Gamma_{\text{left}}$  and  $\Gamma_{\text{top}}$  are unavailable (Figure 3). This missing information renders the forward problem ill-posed, constituting classical schemes relying on *black-box* solvers unusable. In contrast, our method treats the solution field of the PDE (i.e., the displacements in our case) as a random variable, irrespective of whether it pertains to the boundary or the interior of the problem domain, and infers it from the noisy observations and the weighted residuals.

The posterior mean and standard deviation of the unknown material field  $m$  are depicted in Figure 9 for  $SNR = 30dB$ , which should be compared with the results in the second row of Figure 8 that were obtained assuming given Dirichlet boundary conditions. The agreement is good in terms of the mean and the ground truth, but the posterior variance is at times larger due to the additional uncertainty. In Figure 10, we depict slices of the inferred displacements along the aforementioned boundaries  $\Gamma_{\text{left}}$  and  $\Gamma_{\text{top}}$ . One observes that these approximate the ground truth values which are always enveloped by the posterior credible intervals. In addition, the computational effort associated with this case was identical to that for the case where the DIRICHLET BCs were prescribed.

#### 4.5 Comparison for non-linear material

Several studies have shown that human tissue exhibits non-linear material behavior [57, 77]. To this end, we consider a nonlinear, Neo-Hookean constitutive law of the form [78]:

$$\sigma = 2CJ^{-1}(FF^T - I) + (2D(J - 1)) \otimes I, \quad (33)$$

where  $F = (I + \nabla u)$  denotes the deformation gradient,  $J = \det(F)$  is its determinant,  $I$  is the identity matrix, and  $C, D$  are constitutive parameters. We assume that

$$C(\mathbf{s}) = \frac{\tilde{E}}{4(1 + \tilde{\nu})} \quad \text{and} \quad D(\mathbf{s}) = \frac{\tilde{E}\tilde{\nu}}{2(1 + \tilde{\nu})(1 - \tilde{\nu})}, \quad (34)$$

and for  $\tilde{\nu} = 0.45$ , we attempt to infer the spatially varying field  $m(\mathbf{s}) = \log(\tilde{E}(\mathbf{s}))$ . The ground truth is assumed to be the field in Equation (31).

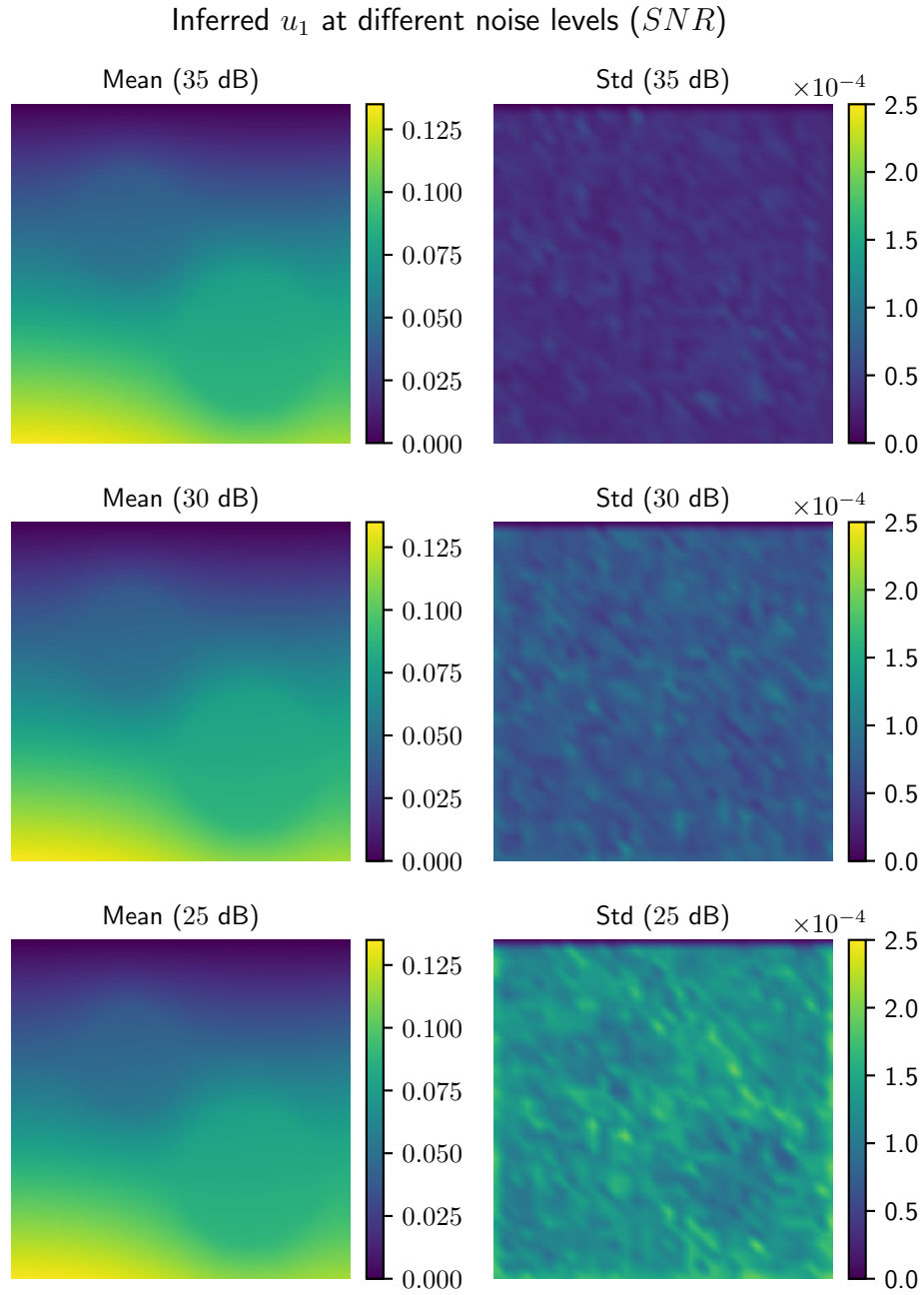


Figure 6: Posterior mean (left column) and standard deviation (right column) for the displacement field  $u_1$  for  $SNR = \{25 \text{ dB}, 30 \text{ dB}, 35 \text{ dB}\}$ . Note that the higher the SNR is, the less noise is present in the data.

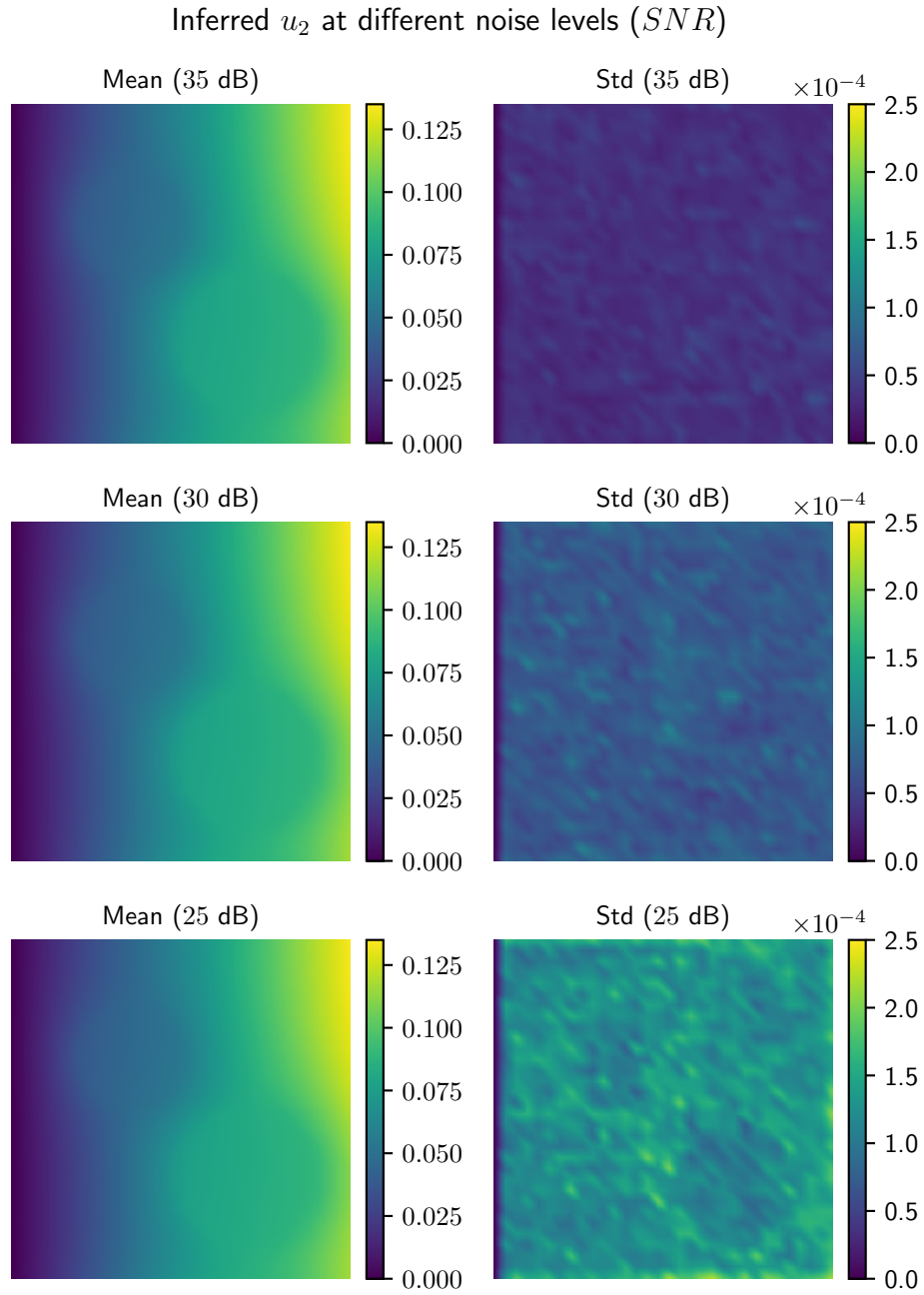


Figure 7: Posterior mean (left column) and standard deviation (right column) for the displacement field  $u_2$  for  $SNR = \{25 \text{ dB}, 30 \text{ dB}, 35 \text{ dB}\}$ . Note that the higher the SNR is, the less noise is present in the data.

Inferred  $\log(E)$  at different noise levels ( $SNR$ )

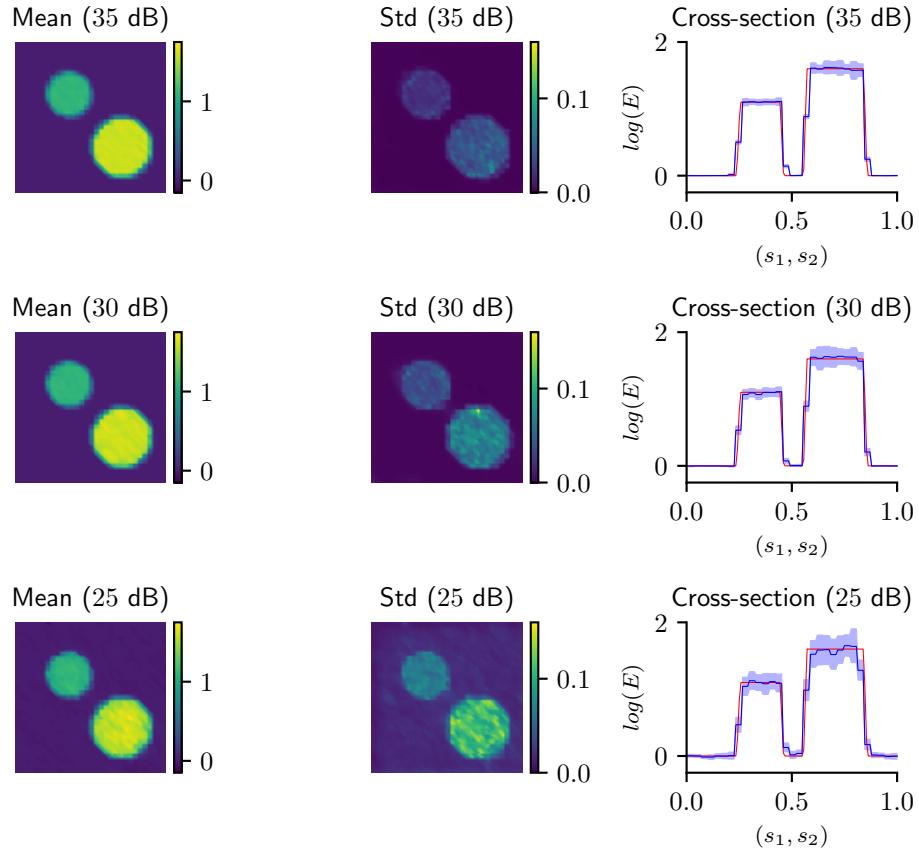


Figure 8: Posterior mean (left column), standard deviation (middle column) and posterior estimates along  $s_1 = s_2$  in the problem domain  $\Omega$  (right column - posterior mean  $\mu$  (blue line) and 95% credible intervals (blue shaded area)) of the logarithm of Young's modulus field for  $SNR = \{25 \text{ dB}, 30 \text{ dB}, 35 \text{ dB}\}$  (1. to 3. row), respectively. Note that the higher the  $SNR$  is, the less noise is present in the data.

Inferred Young modulus  $\log(E)$  (without Dirichlet BCs)

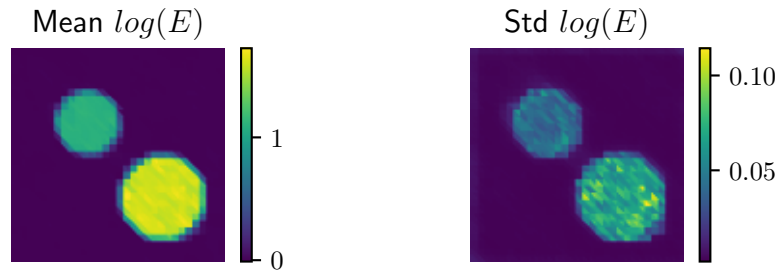


Figure 9: Inferred logarithmic YOUNGS modulus mean and standard deviation fields when the DIRICHLET boundary conditions are not given explicitly for  $SNR = 30 \text{ dB}$ .

### Inferred displacements on boundaries (without Dirichlet BCs)

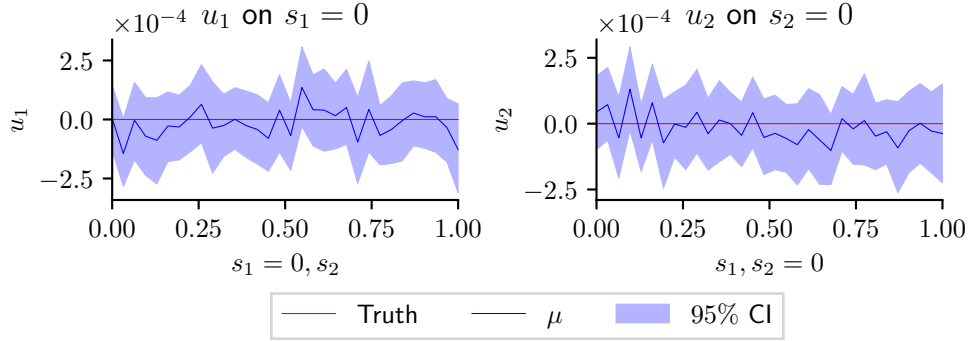


Figure 10: Inferred displacements on the DIRICHLET boundaries when the DIRICHLET boundary conditions are not given explicitly for SNR= 30 dB. Depicted are the inferred mean  $\mu$  (blue line) and 95% credible intervals (blue shaded areas) and the ground truth (red line).

The presence of nonlinearity would necessitate the alteration of the forward solver in a black-box formulation, and each solution would generally imply an increased computational cost as compared to a linear model. In contrast, the only alteration in the proposed formulation pertains to incorporating the constitutive law in the weighted residual computations of Equation (8). Its derivatives are automatically computed using automatic differentiation modules [64].

The posterior mean of the inferred  $m$  and the cross-sections obtained by the proposed method are shown in Figure 11. The accuracy of the posterior estimates is comparable to the previous cases where a linear model was employed. In all cases, the posterior mean is very close to the ground truth, which is largely enveloped by the credible intervals. More importantly, the computational cost to convergence was identical to that for a linear constitutive law. The fact that the inverse problem can be accommodated without any drastic changes in the solution procedure is a significant advantage to classical *black-box* solver-based schemes, which also require increased computational efforts for such non-linear problems.

## 5 Conclusions

We introduced a novel, data-driven method called Weak Neural Variational Inference (WNVI) for solving high-dimensional inverse problems based on PDEs as those arising in the context of model-based elastography. This method solves the inverse problem within a Bayesian framework, i.e., it provides probabilistic estimates of the solution rather than point estimates, which is significant for applications requiring uncertainty quantification. The method employs a physics-aware probabilistic learning objective composed of real observations obtained from actual measurements and virtual observations derived from the weighted residuals of the governing PDE which are used as informational probes. As a result, information from the governing physical equations can be utilized *without* formulating or ever solving the forward problem. The formulation, apart from the usual unknowns, treats the state variables of the physical model as latent variables that are inferred using Stochastic

## Inferred Young modulus $E$ for Neo-Hookean material model

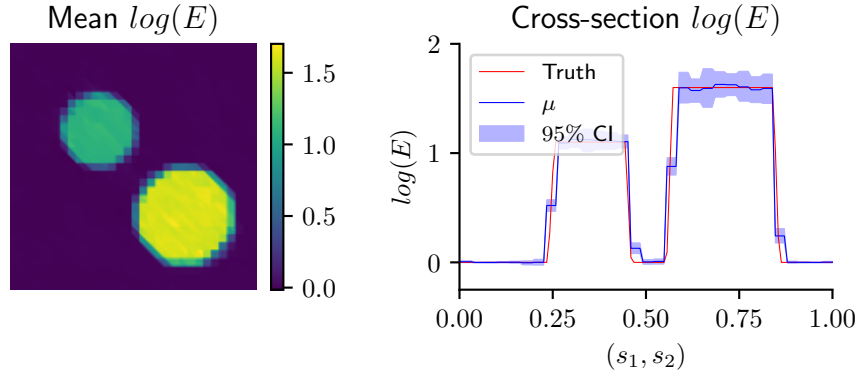


Figure 11: Inferred logarithmic material field  $m$  cross-section (left) and mean field (right) for a non-linear Neo-Hooke material law and SNR= 30 dB. In the cross-section depicted are the inferred mean  $\mu$  (blue line) with 95% credibility intervals (blue regions) and the ground truth (red line).

Variational Inference (SVI). The approximate posterior employed approximates the inverse map, from state variables to the unknowns, with the help of neural networks. As demonstrated in the numerical experiments conducted, the proposed method exhibits several competitive advantages, which we summarize below:

1. Each update in the SVI scheme requires evaluating a limited number of weighted residuals (i.e., integrals over the problem domain) and their derivatives, which can be readily obtained through automatic differentiation. Hence, the forward model *never* needs to be solved, leading to a highly efficient and flexible scheme.
2. Despite the reduced computational cost, the posterior estimates it produces exhibit similar accuracy with those obtained by an asymptotically exact Hamiltonian Monte Carlo (HMC) simulation, which employs the forward and adjoint solver as black-boxes. In practice, this simplifies the use of the method for medical practitioners, who generally do not have the expertise to set up a (nonlinear), discretized, forward model and its adjoint. This can significantly enhance the permeation of model-based in medical diagnostics and significantly simplify and expedite the computations required.
3. It can successfully infer the unknowns not only for ill-posed inverse problems but also for *ill-posed forward problems* as, e.g., those arising when insufficient Dirichlet boundary conditions are prescribed. This addresses a common problem in elastography as boundary conditions are frequently ambiguous or completely unknown in *in vivo* conditions.
4. It can handle nonlinear problems without methodological changes (apart from the integration module in calculating the weighted residuals) or incurring additional computational costs. In the case of elastography, nonlinear problems often arise from the nonlinear material behavior of human tissue.

Moreover, the WNVI framework opens up numerous methodological and application possibilities, detailed below. On the first front, the framework could benefit from a tempering scheme that

progressively increases the precision  $\lambda$  corresponding to the virtual observables or by employing alternative forms of virtual likelihoods to accelerate convergence. Secondly, given the role of the weighting functions as information probes to the governing PDE, one can imagine that their informational content can vary significantly. This can be quantified in the probabilistic framework advocated using the Evidence Lower Bound (ELBO). As a result, the method's efficiency could be greatly enhanced by adaptively adjusting the weighting functions/residuals to maximize informational gain. The potential speed-up by both previously proposed extensions could be vital in practice as it addresses computational scalability issues and draw nearer to real-time, diagnostic capabilities even in cases where inexpensive, hand-held ultrasound devices are used.

We note finally that the proposed method, as all model-based strategies, assumes that the governing equations are correct and reliable. In the context of the PDE-based models of continuum thermodynamics employed in this work, this is true for the conservation laws but not necessarily for constitutive laws. While the method would always produce estimates of the unknown material parameters, those would be incorrect if the constitutive relation is invalid. In the context of model-based elastography this can lead to erroneous diagnostic decisions by the medical practitioners. It would be beneficial therefore to be able to identify regions where the proposed constitutive equations are insufficient to model the material behavior. The framework advocated in this paper can be extended to incorporate different types of governing equations separately by employing different sets of virtual observables in order to achieve such a modification.

## **Acknowledgement**

The support of the Deutsche Forschungsgemeinschaft (DFG) through Project Number 499746055 is gratefully acknowledged.



## References

- [1] Avinash C Kak and Malcolm Slaney. *Principles of computerized tomographic imaging*. SIAM, 2001.
- [2] Charles Jackson, Mrinal K Sen, and Paul L Stoffa. “An efficient stochastic Bayesian approach to optimal parameter and uncertainty estimation for climate model predictions”. In: *Journal of Climate* 17.14 (2004), pp. 2828–2841.
- [3] Mary C Hill and Claire R Tiedeman. *Effective groundwater model calibration: with analysis of data, sensitivities, predictions, and uncertainty*. John Wiley & Sons, 2006.
- [4] Ian Craig and John Brown. “Inverse problems in astronomy”. In: (1986).
- [5] Marvin M Dooley. “Model-based elastography: a survey of approaches to the inverse elasticity problem”. In: *Physics in Medicine & Biology* 57.3 (2012), R35.
- [6] Nathalie Ganne-Carrié et al. “Accuracy of liver stiffness measurement for the diagnosis of cirrhosis in patients with chronic liver diseases”. en. In: *Hepatology* 44.6 (Dec. 2006), pp. 1511–1517. ISSN: 02709139, 15273350. DOI: 10.1002/hep.21420. URL: <https://onlinelibrary.wiley.com/doi/10.1002/hep.21420> (visited on 03/24/2023).
- [7] Ahmed M. Sayed et al. “Breast Tumor Diagnosis Using Finite-Element Modeling Based on Clinical in vivo Elastographic Data”. en. In: *Journal of Ultrasound in Medicine* 39.12 (Dec. 2020), pp. 2351–2363. ISSN: 0278-4297, 1550-9613. DOI: 10.1002/jum.15344. URL: <https://onlinelibrary.wiley.com/doi/10.1002/jum.15344> (visited on 03/24/2023).
- [8] Kenneth Hoyt et al. “Tissue elasticity properties as biomarkers for prostate cancer”. en. In: *Cancer Biomarkers* 4.4-5 (Nov. 2008). Ed. by Ernest J. Feleppa, pp. 213–225. ISSN: 18758592, 15740153. DOI: 10.3233/CBM-2008-44-505. URL: <https://www.medra.org/servlet/aliasResolver?alias=iospress&doi=10.3233/CBM-2008-44-505> (visited on 03/24/2023).
- [9] Patrick Asbach et al. “Assessment of liver viscoelasticity using multifrequency MR elastography”. en. In: *Magnetic Resonance in Medicine* 60.2 (Aug. 2008), pp. 373–379. ISSN: 07403194, 15222594. DOI: 10.1002/mrm.21636. URL: <https://onlinelibrary.wiley.com/doi/10.1002/mrm.21636> (visited on 03/24/2023).
- [10] Uwe Hamhaber et al. “In vivo magnetic resonance elastography of human brain at 7 T and 1.5 T”. en. In: *Journal of Magnetic Resonance Imaging* 32.3 (Aug. 2010), pp. 577–583. ISSN: 10531807. DOI: 10.1002/jmri.22294. URL: <https://onlinelibrary.wiley.com/doi/10.1002/jmri.22294> (visited on 03/24/2023).
- [11] Jacques Ohayon et al. “Biomechanics of Atherosclerotic Coronary Plaque: Site, Stability and In Vivo Elasticity Modeling”. en. In: *Annals of Biomedical Engineering* 42.2 (Feb. 2014), pp. 269–279. ISSN: 0090-6964, 1573-9686. DOI: 10.1007/s10439-013-0888-1. URL: <http://link.springer.com/10.1007/s10439-013-0888-1> (visited on 03/24/2023).
- [12] Spencer W. Shore et al. “Transversely Isotropic Elasticity Imaging of Cancellous Bone”. en. In: *Journal of Biomechanical Engineering* 133.6 (June 2011), p. 061002. ISSN: 0148-0731, 1528-8951. DOI: 10.1115/1.4004231. URL: <https://asmedigitalcollection.asme>.

- org/biomechanical/article/doi/10.1115/1.4004231/470019/Transversely-Isotropic-Elasticity-Imaging-of (visited on 03/24/2023).
- [13] Cédric Schmitt et al. “Noninvasive Vascular Elastography: Toward A Complementary Characterization Tool of Atherosclerosis in Carotid Arteries”. en. In: *Ultrasound in Medicine & Biology* 33.12 (Dec. 2007), pp. 1841–1858. ISSN: 03015629. DOI: 10.1016/j.ultrasmedbio.2007.05.020. URL: <https://linkinghub.elsevier.com/retrieve/pii/S0301562907002694> (visited on 03/24/2023).
- [14] Paul E Barbone and Nachiket H Gokhale. “Elastic modulus imaging: on the uniqueness and nonuniqueness of the elastography inverse problem in two dimensions”. In: *Inverse problems* 20.1 (2004), p. 283.
- [15] Joyce R McLaughlin and Jeong-Rock Yoon. “Unique identifiability of elastic parameters from time-dependent interior displacement measurement”. In: *Inverse Problems* 20.1 (2003), p. 25.
- [16] Paul E Barbone and Jeffrey C Bamber. “Quantitative elasticity imaging: what can and cannot be inferred from strain images”. In: *Physics in Medicine & Biology* 47.12 (2002), p. 2147.
- [17] Albert Tarantola. *Inverse problem theory and methods for model parameter estimation*. SIAM, 2005.
- [18] Jari Kaipio and Erkki Somersalo. *Statistical and computational inverse problems*. Vol. 160. Springer Science & Business Media, 2006.
- [19] Peter J Green et al. “Bayesian computation: a summary of the current state, and samples backwards and forwards”. In: *Statistics and Computing* 25 (2015), pp. 835–862.
- [20] P.S. Koutsourelakis. “A multi-resolution, non-parametric, Bayesian framework for identification of spatially-varying model parameters”. In: *Journal of Computational Physics* 228.17 (Sept. 2009), pp. 6184–6211. ISSN: 0021-9991. DOI: 10.1016/j.jcp.2009.05.016. URL: <http://dx.doi.org/10.1016/j.jcp.2009.05.016>.
- [21] David M Blei, Alp Kucukelbir, and Jon D McAuliffe. “Variational inference: A review for statisticians”. In: *Journal of the American statistical Association* 112.518 (2017), pp. 859–877.
- [22] Gareth O Roberts and Richard L Tweedie. “Exponential convergence of Langevin distributions and their discrete approximations”. In: *Bernoulli* (1996), pp. 341–363.
- [23] Jonathan C Mattingly, Natesh S Pillai, and Andrew M Stuart. “Diffusion limits of the random walk Metropolis algorithm in high dimensions”. In: (2012).
- [24] Alessio Spantini, Daniele Bigoni, and Youssef Marzouk. “Inference via low-dimensional couplings”. In: *The Journal of Machine Learning Research* 19.1 (Jan. 2018), pp. 2639–2709. ISSN: 1532-4435.
- [25] Isabell M Franck and PS Koutsourelakis. “Sparse Variational Bayesian approximations for nonlinear inverse problems: Applications in nonlinear elastography”. In: *Computer Methods in Applied Mechanics and Engineering* 299 (2016), pp. 215–244.
- [26] Jinglai Li and Youssef M. Marzouk. “Adaptive Construction of Surrogates for the Bayesian Solution of Inverse Problems”. In: *SIAM Journal on Scientific Computing* 36.3 (Jan. 2014), A1163–A1186. ISSN: 1095-7197. DOI: 10.1137/130938189. URL: <http://dx.doi.org/10.1137/130938189>.

- [27] Youssef M. Marzouk, Habib N. Najm, and Larry A. Rahn. “Stochastic spectral methods for efficient Bayesian solution of inverse problems”. In: *Journal of Computational Physics* 224.2 (June 2007), pp. 560–586. ISSN: 0021-9991. DOI: 10.1016/j.jcp.2006.10.010. URL: <http://dx.doi.org/10.1016/j.jcp.2006.10.010>.
- [28] Chen Chen and Qifeng Liao. “ANOVA Gaussian process modeling for high-dimensional stochastic computational models”. In: *Journal of Computational Physics* 416 (Sept. 2020), p. 109519. ISSN: 0021-9991. DOI: 10.1016/j.jcp.2020.109519. URL: <http://dx.doi.org/10.1016/j.jcp.2020.109519>.
- [29] Ilias Bilonis et al. “Multi-output separable Gaussian process: Towards an efficient, fully Bayesian paradigm for uncertainty quantification”. In: *Journal of Computational Physics* 241 (May 2013), pp. 212–239. ISSN: 0021-9991. DOI: 10.1016/j.jcp.2013.01.011. URL: <http://dx.doi.org/10.1016/j.jcp.2013.01.011>.
- [30] Sheroze Sherifdeen et al. “Accelerating PDE-constrained Inverse Solutions with Deep Learning and Reduced Order Models”. In: *arXiv:1912.08864 [physics, stat]* (Dec. 2019). arXiv: 1912.08864. URL: <http://arxiv.org/abs/1912.08864> (visited on 09/01/2021).
- [31] Ke Li et al. “A Hierarchical Neural Hybrid Method for Failure Probability Estimation”. In: *IEEE Access* 7 (2019), pp. 112087–112096. ISSN: 2169-3536. DOI: 10.1109/access.2019.2934980. URL: <http://dx.doi.org/10.1109/ACCESS.2019.2934980>.
- [32] Yinhao Zhu and Nicholas Zabaras. “Bayesian deep convolutional encoder–decoder networks for surrogate modeling and uncertainty quantification”. In: *Journal of Computational Physics* 366 (Aug. 2018), pp. 415–447. ISSN: 0021-9991. DOI: 10.1016/j.jcp.2018.04.018. URL: <http://dx.doi.org/10.1016/j.jcp.2018.04.018>.
- [33] Shaoxing Mo et al. “Deep convolutional encoder-decoder networks for uncertainty quantification of dynamic multiphase flow in heterogeneous media”. In: *Water Resources Research* 55.1 (2019), pp. 703–728.
- [34] Zongyi Li et al. “Fourier neural operator for parametric partial differential equations”. In: *arXiv preprint arXiv:2010.08895* (2020).
- [35] Lu Lu, Pengzhan Jin, and George Em Karniadakis. “Deeponet: Learning nonlinear operators for identifying differential equations based on the universal approximation theorem of operators”. In: *arXiv preprint arXiv:1910.03193* (2019).
- [36] Sebastian Kaltenbach, Paris Perdikaris, and Phaedon-Stelios Koutsourelakis. “Semi-supervised invertible neural operators for Bayesian inverse problems”. In: *Computational Mechanics* 72.3 (2023), pp. 451–470.
- [37] Benjamin Peherstorfer, Karen Willcox, and Max Gunzburger. “Survey of Multifidelity Methods in Uncertainty Propagation, Inference, and Optimization”. In: *SIAM Review* 60.3 (Jan. 2018), pp. 550–591. ISSN: 1095-7200. DOI: 10.1137/16m1082469. URL: <http://dx.doi.org/10.1137/16M1082469>.
- [38] Liang Yan and Tao Zhou. “Adaptive multi-fidelity polynomial chaos approach to Bayesian inference in inverse problems”. In: *Journal of Computational Physics* 381 (Mar. 2019), pp. 110–128. ISSN: 0021-9991. DOI: 10.1016/j.jcp.2018.12.025. URL: <http://dx.doi.org/10.1016/j.jcp.2018.12.025>.

- [39] Jonas Nitzler et al. “A generalized probabilistic learning approach for multi-fidelity uncertainty propagation in complex physical simulations”. In: *arXiv preprint arXiv:2001.02892* (2020).
- [40] Govinda Anantha Padmanabha and Nicholas Zabarar. “Solving inverse problems using conditional invertible neural networks”. In: *Journal of Computational Physics* 433 (2021), p. 110194.
- [41] I Billionis and N Zabarar. “Solution of inverse problems with limited forward solver evaluations: a Bayesian perspective”. In: *Inverse Problems* 30.1 (Dec. 2013), p. 015004. ISSN: 1361-6420. DOI: 10.1088/0266-5611/30/1/015004. URL: <http://dx.doi.org/10.1088/0266-5611/30/1/015004>.
- [42] Maziar Raissi, Paris Perdikaris, and George E Karniadakis. “Physics-informed neural networks: A deep learning framework for solving forward and inverse problems involving nonlinear partial differential equations”. In: *Journal of Computational physics* 378 (2019), pp. 686–707.
- [43] Gang Bao et al. “Numerical solution of inverse problems by weak adversarial networks”. In: *Inverse Problems* 36.11 (2020), p. 115003.
- [44] Yaohua Zang et al. “Weak adversarial networks for high-dimensional partial differential equations”. In: *Journal of Computational Physics* 411 (2020), p. 109409.
- [45] Zongyi Li et al. “Physics-informed neural operator for learning partial differential equations”. In: *ACM/JMS Journal of Data Science* (2021).
- [46] Aditi Krishnapriyan et al. “Characterizing possible failure modes in physics-informed neural networks”. In: *Advances in Neural Information Processing Systems* 34 (2021), pp. 26548–26560.
- [47] Liu Yang, Xuhui Meng, and George Em Karniadakis. “B-PINNs: Bayesian physics-informed neural networks for forward and inverse PDE problems with noisy data”. In: *Journal of Computational Physics* 425 (2021), p. 109913.
- [48] Xu Liu et al. “Bayesian physics-informed extreme learning machine for forward and inverse PDE problems with noisy data”. In: *Neurocomputing* 549 (2023), p. 126425.
- [49] Phaedon-Stelios Koutsourelakis. “A novel Bayesian strategy for the identification of spatially varying material properties and model validation: an application to static elastography”. In: *International Journal for Numerical Methods in Engineering* 91.3 (2012), pp. 249–268.
- [50] Lukas Bruder and Phaedon-Stelios Koutsourelakis. “Beyond black-boxes in Bayesian inverse problems and model validation: applications in solid mechanics of elastography”. In: *International Journal for Uncertainty Quantification* 8.5 (2018).
- [51] Sebastian Kaltenbach and Phaedon-Stelios Koutsourelakis. “Incorporating physical constraints in a deep probabilistic machine learning framework for coarse-graining dynamical systems”. In: *Journal of Computational Physics* 419 (2020), p. 109673.
- [52] Maximilian Rixner and Phaedon-Stelios Koutsourelakis. “A probabilistic generative model for semi-supervised training of coarse-grained surrogates and enforcing physical constraints through virtual observables”. In: *Journal of Computational Physics* 434 (2021), p. 110218.
- [53] Arnaud Vadeboncoeur et al. “Fully probabilistic deep models for forward and inverse problems in parametric PDEs”. In: *Journal of Computational Physics* 491 (2023), p. 112369.

- [54] Yinhao Zhu et al. “Physics-constrained deep learning for high-dimensional surrogate modeling and uncertainty quantification without labeled data”. en. In: *Journal of Computational Physics* 394 (Oct. 2019), pp. 56–81. ISSN: 0021-9991. DOI: 10.1016/j.jcp.2019.05.024. URL: <http://www.sciencedirect.com/science/article/pii/S0021999119303559> (visited on 10/30/2020).
- [55] Assad A Oberai et al. “Linear and nonlinear elasticity imaging of soft tissue in vivo: demonstration of feasibility”. In: *Physics in Medicine & Biology* 54.5 (2009), p. 1191.
- [56] AA Oberai et al. “Evaluation of the adjoint equation based algorithm for elasticity imaging”. In: *PHYSICS IN MEDICINE AND BIOLOGY* 49.13 (July 2004), pp. 2955–2974. ISSN: 0031-9155. DOI: 10.1088/0031-9155/49/13/.
- [57] Assad A. Oberai et al. “Linear and nonlinear elasticity imaging of soft tissue in vivo: demonstration of feasibility”. In: *PHYSICS IN MEDICINE AND BIOLOGY* 54.5 (Mar. 2009), pp. 1191–1207. ISSN: 0031-9155. DOI: 10.1088/0031-9155/54/5/006.
- [58] V. S. Fanaskov and I. V. Oseledets. “Spectral Neural Operators”. en. In: *Doklady Mathematics* 108.2 (Dec. 2023), S226–S232. ISSN: 1531-8362. DOI: 10.1134/S1064562423701107. URL: <https://doi.org/10.1134/S1064562423701107> (visited on 05/06/2024).
- [59] Ted Belytschko et al. *Nonlinear finite elements for continua and structures*. John wiley & sons, 2014.
- [60] Bruce A Finlayson. *The method of weighted residuals and variational principles*. SIAM, 2013.
- [61] Ehsan Kharazmi, Zhongqiang Zhang, and George Em Karniadakis. “hp-VPINNs: Variational physics-informed neural networks with domain decomposition”. In: *Computer Methods in Applied Mechanics and Engineering* 374 (2021), p. 113547.
- [62] Matthew D Hoffman et al. “Stochastic variational inference”. In: *Journal of Machine Learning Research* (2013).
- [63] Diederik P Kingma and Max Welling. “Auto-encoding variational bayes”. In: *arXiv preprint arXiv:1312.6114* (2013).
- [64] Adam Paszke et al. “PyTorch: An Imperative Style, High-Performance Deep Learning Library”. In: *Advances in Neural Information Processing Systems* 32. Curran Associates, Inc., 2019, pp. 8024–8035. URL: <http://papers.nips.cc/paper/9015-pytorch-an-imperative-style-high-performance-deep-learning-library.pdf>.
- [65] Christopher M Bishop. “Pattern recognition and machine learning”. In: *Springer google schola* 2 (2006), pp. 1122–1128.
- [66] Martin Alnæs et al. “The FEniCS project version 1.5”. In: *Archive of numerical software* 3.100 (2015).
- [67] Anders Logg, Kent-Andre Mardal, and Garth Wells. *Automated solution of differential equations by the finite element method: The FEniCS book*. Vol. 84. Springer Science & Business Media, 2012.
- [68] Sebastian Mitusch, Simon Funke, and Jørgen Dokken. “dolfin-adjoint 2018.1: automated adjoints for FEniCS and Firedrake”. In: *Journal of Open Source Software* 4.38 (2019), p. 1292.
- [69] Johnathan M Bardsley and Jari Kaipio. “GAUSSIAN MARKOV RANDOM FIELD PRIORS FOR INVERSE PROBLEMS.” In: *Inverse Problems & Imaging* 7.2 (2013).

- [70] Christopher M Bishop and Michael Tipping. “Variational relevance vector machines”. In: *arXiv preprint arXiv:1301.3838* (2013).
- [71] Diederik P Kingma and Jimmy Ba. “Adam: A method for stochastic optimization”. In: *arXiv preprint arXiv:1412.6980* (2014).
- [72] Thomas R Cox and Janine T Erler. “Remodeling and homeostasis of the extracellular matrix: implications for fibrotic diseases and cancer”. In: *Disease models & mechanisms* 4.2 (2011), pp. 165–178.
- [73] Matthew W Conklin and Patricia J Keely. “Why the stroma matters in breast cancer: insights into breast cancer patient outcomes through the examination of stromal biomarkers”. In: *Cell adhesion & migration* 6.3 (2012), pp. 249–260.
- [74] Parris Wellman et al. “Breast tissue stiffness in compression is correlated to histological diagnosis”. In: *Harvard BioRobotics Laboratory Technical Report 1* (1999).
- [75] Sebastian Mueller and Laurent Sandrin. “Liver stiffness: a novel parameter for the diagnosis of liver disease”. In: *Hepatic medicine: evidence and research* (2010), pp. 49–67.
- [76] Ryota Masuzaki et al. “Assessing liver tumor stiffness by transient elastography”. In: *Hepatology international* 1 (2007), pp. 394–397.
- [77] Joseph J O’Hagan and Abbas Samani. “Measurement of the hyperelastic properties of 44 pathological ex vivo breast tissue samples”. In: *Physics in Medicine & Biology* 54.8 (2009), p. 2557.
- [78] Raymond W Ogden. *Non-linear elastic deformations*. Courier Corporation, 1997.
- [79] Prajit Ramachandran, Barret Zoph, and Quoc V Le. “Searching for activation functions”. In: *arXiv preprint arXiv:1710.05941* (2017).

## A Numerical integration

While general numerical integration techniques can be used for the integrals appearing in the weighted residuals in Equation (8), we employed a method adapted to the particular feature functions used (see Equation (7)) in the numerical illustrations. In particular and given that these were associated with a uniform, triangle mesh, we used closed form expressions over each triangle and summed over all of them in order to obtain the final result.

## B ELBO Terms

We selected an uninformative Gaussian prior  $p(\mathbf{y}) = \mathcal{N}(\mathbf{y} | \mathbf{0}, \sigma^2 \mathbf{I})$ , where  $\sigma^2 = 10^{16}$  (see section 4.1). We applied a prior on  $\mathbf{x}$  that penalizes jumps between neighboring elements with penalty precision  $\theta$  as in Equation (30), which must also be inferred. We adopt a mean-field approximation where the approximate posterior is of the form  $q(\mathbf{x}, \mathbf{y}, \theta) = q_{\xi}(\mathbf{x}, \mathbf{y})q(\theta)$ . The approximate posterior  $q_{\xi}(\mathbf{y}, \mathbf{x}) = q(\mathbf{x} | \mathbf{y})q(\mathbf{y})$  consists of multivariate Gaussians with low-rank approximations of the covariance matrix and the mean of  $q_{\xi}(\mathbf{x} | \mathbf{y})$  is represented via a neural network (see subsection 3.3). The approximate posterior  $q(\theta)$  is a Gamma distribution updates for which can be obtained in closed form. Substituting the Monte Carlo approximation of the virtual likelihood term in Equation (15)

into ELBO formulation in Equation (14) yields in general

$$\begin{aligned}
\mathcal{L}(\xi) &\approx -\lambda \frac{N}{K} \sum_{k=1}^K \langle r_{\mathbf{w}^{j_k}}^2(\mathbf{y}, \mathbf{x}) \rangle_{q_\xi(\mathbf{y}, \mathbf{x}, \boldsymbol{\theta})} \\
&\quad - \frac{\tau}{2} \sum_{i=1}^N \langle (\hat{\mathbf{u}}_i - \mathbf{u}_i(\mathbf{y}))^2 \rangle_{q_\xi(\mathbf{y}, \mathbf{x}, \boldsymbol{\theta})} \\
&\quad + \langle \log p(\mathbf{y}, \mathbf{x}, \boldsymbol{\theta}) \rangle_{q_\xi(\mathbf{y}, \mathbf{x}, \boldsymbol{\theta})} \\
&\quad - \langle \log q_\xi(\mathbf{y}, \mathbf{x}, \boldsymbol{\theta}) \rangle_{q_\xi(\mathbf{y}, \mathbf{x}, \boldsymbol{\theta})} \text{ where } j_k \sim \text{Cat} \left( N, \frac{1}{N} \right). \tag{35}
\end{aligned}$$

We note that the ELBO depends on the product  $\lambda N$  rather than the individual terms which in the sequel **we represent simply as  $\lambda$** . Hence, in the sequel, the ELBO is approximated using the reparameterization trick [63]. We can thus sample tuples  $\{\mathbf{x}_\ell, \mathbf{y}_\ell\}_{\ell=1}^L$  from the approximate posterior  $q_\xi(\mathbf{x}, \mathbf{y})$  as described in subsection 3.4 and use those calculate a Monte Carlo estimate of the expectations in Equation (35). Sampling from  $q(\boldsymbol{\theta})$  is not necessary, as we can update the posterior and calculate the needed expectations in closed form (see Appendix D). Thus, Equation (35) can be rewritten (up to an additive constant)

$$\begin{aligned}
\mathcal{L}(\xi) &\approx -\lambda \frac{1}{KL} \sum_{k=1}^K \sum_{\ell=1}^L r_{\mathbf{w}^{j_k}}^2(\mathbf{y}_\ell, \mathbf{x}_\ell) \\
&\quad - \frac{\tau}{2L} \sum_{i=1}^{N\hat{u}} \sum_{\ell=1}^L (\hat{\mathbf{u}}_i - \mathbf{u}_i(\mathbf{y}_\ell))^2 \\
&\quad - \frac{1}{2L} \sum_{\ell=1}^L \mathbf{y}_\ell^T \left( \frac{1}{\sigma^2} \mathbf{I} \right) \mathbf{y}_\ell \\
&\quad - \frac{1}{2L} \sum_{\ell=1}^L (\mathbf{L}\mathbf{x}_\ell)^T \text{diag}(\langle \boldsymbol{\theta} \rangle) (\mathbf{L}\mathbf{x}_\ell) \\
&\quad + \log \left( \langle \boldsymbol{\theta} \rangle^{a_0-1} \right) - b_0 \langle \boldsymbol{\theta} \rangle \\
&\quad - \frac{1}{2} \log \det (\mathbf{S}_y) \\
&\quad - \frac{1}{2} \log \det (\mathbf{S}_x) \\
&\quad + \sum_{i=1}^I (-a_{\theta_i} + \log b_{\theta_i} - \log \Gamma(a_{\theta_i}) - (1 - a_{\theta_i})\psi(a_{\theta_i})), \tag{36}
\end{aligned}$$

where we get  $\langle \boldsymbol{\theta} \rangle = \frac{a_{\theta_i}}{b_{\theta_i}}$  with Equation (38). The third term can be ignored since we employ a large  $\sigma$  in the uninformative prior of  $\mathbf{y}$ . As discussed in Appendix D, we can iterate between first updating the approximate posterior  $q(\boldsymbol{\theta})$  in closed form and then updating the approximate posterior  $q(\mathbf{x}, \mathbf{y})$  using the derivatives of the ELBO in Equation (36) obtained via automatic differentiation.

## C Neural Network details

The conditional mean  $\boldsymbol{\mu}_{\mathbf{x}, \xi_x}$  of the approximate conditional posterior  $q_\xi(\mathbf{x}|\mathbf{y})$  in Equation (17) is parametrized by a neural network with tunable parameters  $\xi_x$ . While virtually any neural network

architecture is viable (e.g., CNN, deepONet, Deep Neural Network), we select a fully connected feed-forward neural network. For all our experiments we take the  $d_{\mathbf{y}}$ -dimensional input vector  $\mathbf{y}$  and pass them through three sequential hidden layers with 2000 neurons each and apply a SiLU (or Swish [79]) activation function given by

$$\text{SiLU}(x) = x\sigma(x), \quad (37)$$

where  $\sigma(x)$  denotes the sigmoid function. The last hidden layer is connected to the  $d_{\mathbf{x}}$ -dimensional output layer, which yields the conditional mean  $\boldsymbol{\mu}_{\mathbf{x}}$ . We do not claim this design choice to be optimal in hyperparameter selection or architecture. Further studies can be conducted.

## D Jump penalty prior

To find a solution field with constant inclusions in a constant background, we employ a prior on  $\mathbf{x}$  that penalizes jumps between neighboring elements as given in Eq. (30). Here, we model the prior by a normal distribution where the mean is zero (i.e., no jumps), and the penalty for all jumps are given by a precision vector  $\boldsymbol{\theta}$ . The jump penalties  $\boldsymbol{\theta}$  have a Gamma hyperprior, and we thus have to infer them in our approximate posterior. Note that the normal prior and the Gamma hyperprior are *conjugate*, and we get a Gamma approximate posterior as a natural choice. We can, thus, update the approximate posterior in closed form as

$$a_{\theta_i} = a_0 + \frac{1}{2}, \quad \text{and} \quad b_{\theta_i} = b_0 + \frac{1}{2}J_i^2, \quad (38)$$

where  $J_i = (\mathbf{L}\mathbf{x})_i$  is the respective value of the jump. Since the jump  $J_i$  is dependent on  $\mathbf{x}$ , we suggest iterating between

1. Updating the approximate posterior  $q(\boldsymbol{\theta})$  according to Eq. (38) given samples of  $\mathbf{x}$ , and
2. Updating the approximate posterior  $q(\mathbf{y}, \mathbf{x})$  according to the SVI scheme introduced in section 3, where we can calculate  $\langle \boldsymbol{\theta} \rangle = \frac{a_{\theta_i}}{b_{\theta_i}}$  in closed form and the log probability of the prior and hyperprior becomes

$$\log p(\mathbf{J}) = \langle \log p(\mathbf{J}|\boldsymbol{\theta}) \rangle + \left\langle \log \frac{p(\boldsymbol{\theta})}{q(\boldsymbol{\theta})} \right\rangle \quad (39)$$

$$= -\frac{1}{2} \left\langle \mathbf{J}^T \text{diag}(\boldsymbol{\theta}) \mathbf{J} \right\rangle \quad (40)$$

$$= -\frac{1}{2} \left\langle \mathbf{J}^T \right\rangle \text{diag} \left( \frac{a_{\theta_i}}{b_{\theta_i}} \right) \langle \mathbf{J} \rangle. \quad (41)$$

## E Comparison details

The comparison in subsection 4.2 uses the number of weighted residual evaluations as a metric for computational cost. Our method evaluated 200 weight functions for 10  $\mathbf{x} - \mathbf{y}$ -tuples, yielding 2000 residual evaluations per iteration. The method took 200,000 iterations to converge, which amounts to  $4 \times 10^8$  residual evaluations.

To compare black-box solver-based methods to ours, we considered an iterative solver. This requires the calculation of all residuals (2048) over each update of  $\mathbf{y}$  until the desired tolerance (absolute



tolerance of  $10^{-6}$ ) is reached. Starting from an initial vector  $\mathbf{y} = \mathbf{0}$ , this takes on average 4400 updates using the Generalized minimal residual method (GMRES). In HMC, however, subsequent steps yield similar results, and we can use the converged solution from the previous step as the initial guess for the next step. This reduces the number of required updates to 220. This assumption cannot be made for SVI, as we draw independent samples from the posterior. We thus have 450, 560 and 9, 011, 200 weighted residual evaluation equivalents per black-box forward solve for HMC and SVI, respectively. We, therefore, compare the posteriors after 880 and 45 black-box forward solves for HMC and SVI to our approximate posterior, respectively.